TAMPEREEN TEKNILLINEN YLIOPISTO
TAMPERE UNIVERSITY OF TECHNOLOGY

Paola Vivo

Multilayered Thin Films for Organic Photovoltaics

Julkaisu 918 • Publication 918

Tampere 2010

Tampereen teknillinen yliopisto. Julkaisu 918
Tampere University of Technology. Publication 918

Paola Vivo

Multilayered Thin Films for Organic Photovoltaics

Thesis for the degree of Doctor of Science in Technology to be presented with due permission for public examination and criticism in Festia Building, Auditorium Pieni Sali 1, at Tampere University of Technology, on the 29th of October 2010, at 12 noon.

Tampereen teknillinen yliopisto - Tampere University of Technology
Tampere 2010

ISBN 978-952-15-2450-9 (printed)
ISBN 978-952-15-2461-5 (PDF)
ISSN 1459-2045

Abstract

This work investigates the photoinduced interactions between different organic chromophores, thus identifying possible materials for organic photovoltaic applications. The intermolecular electron transfer (ET) in layered structures centered on a covalently bridged porphyrin–fullerene dyad (**P–F**) was studied by means of electrical and spectroscopic methods. When excited, the dyad initiates the vectorial ET in the films, and secondary processes take place after the charge separation between the porphyrin and fullerene moieties of **P–F**. This study showed that violanthrone-79 (**V-79**) and two different perylene derivatives (**PDI** and **PTCDI**) were capable to accept electrons from the photoinduced fullerene anion of **P–F**. Longer-lived electrical and spectroscopic signals were achieved when the film structures were expanded to multilayered configurations containing an electron-donor, the **P–F** dyad, and an electron-acceptor. The electron-donor material used was poly(3-hexylthiophene) (**PHT**).

The film deposition technique was switched from the Langmuir–Blodgett (LB) to Langmuir–Schäfer (LS) or thermal evaporation methods in order to achieve stronger photoelectrical signal amplitudes.

As a result of the information gained in the ET studies, photovoltaic devices were prepared based on the studied compounds. The photocurrent generated from the ultrathin film systems studied in this Thesis can be easily measured with a three-electrode photoelectrochemical cell. In fact, the deposition of a metal top-electrode on the solar cell would damage the underlying organics, thus leading to short-circuiting problems. However, since the liquid cells suffer of poor performances and low stability, it was aimed to build layered cells with a metal top-electrode. The first step in this direction was the optimization of the organics|top-electrode junction, in order to protect the thin organic films. This was achieved with the introduction of a thin tris-8-hydroxy-quinolato aluminum (**Alq_3**) layer in the cell, which successfully enhanced both the efficiency and the lifetime of the devices.

Finally, multilayered cells based on a donor–acceptor pair sandwiched between an electron-donor and an electron-acceptor were developed, demonstrating that it is possible to design photovoltaic devices starting from the valuable information offered by the ET studies. The molecule chosen to this aim was the phthalocyanine-fullerene dyad, **$H_2Pc–C_{60}ee$**, which could be easily deposited as spin-coated layer.

Preface

First and foremost, I wish to thank my supervisor Professor Helge Lemmetyinen for all the guidance and support provided throughout the years. I especially appreciated his belief in the research objectives, which strongly motivated me to achieve my goals. I am also thankful to Professor Nikolai Tkachenko for the fruitful discussions and explanations.

I am particularly indebted to Dr. Vladimir Chukharev. His help during the experiments and in the reviewing of the manuscripts has been indispensable for this Thesis. I am grateful to Dr. Alexander Efimov for synthesizing part of the compounds studied in this work, and for the nice discussions. I wish to thank Dr. Tommi Vuorinen for his guidance, especially in the first year of my research work, and Dr. Kimmo Kaunisto for his support and advices. All the coauthors of the publications deserve acknowledgment. Particularly, I thank Dr. Alexander Alekseev for our fruitful cooperation.

I am thankful to all the colleagues from the Department of Chemistry and Bioengineering for providing me with a pleasant working environment. Especially, I would like to mention my roommates for their continuous help in small and big matters, and for the nice chats during the writing breaks.

I am truly grateful to my parents and to my brother and sister for always being on my side, and for encouraging me during the difficult moments of this work.

My friends from different countries have been essential in the finalizing of this Thesis. Thank you all for the enjoyable and relaxing moments that we have shared.

Above all, my warmest thanks go to my beloved husband Cristiano for his love, support, and enthusiasm in sharing the joyful and hard times of these years.

The research work presented in this Thesis was carried out at the Department of Chemistry and Bioengineering, Tampere University of Technology during the years 2006–2010. The Finnish Funding Agency for Technology and Innovation (TEKES), project ‘Organic Solar Cell’, and the Finnish National Graduate School of Nanoscience are gratefully acknowledged for funding.

Tampere, October 2010 Paola Vivo

Contents

List of publications

The Thesis is based on the work contained in the following publications, which will hereafter be referred to by their Roman numerals:

I **Multicomponent molecularly controlled Langmuir–Blodgett systems for organic photovoltaic applications**
Paola Vivo, Tommi Vuorinen, Vladimir Chukharev, Antti Tolkki, Kimmo Kaunisto, Petri Ihalainen, Jouko Peltonen, and Helge Lemmetyinen
J. Phys. Chem. C **2010**, *114*, 8559.

II **Photoinduced electron transfer in thin films of porphyrin-fullerene dyad and perylenetetracarboxidiimide**
Paola Vivo, Alexander S. Alekseev, Kimmo Kaunisto, Oili Pekkola, Antti Tolkki, Vladimir Chukharev, Alexander Efimov, Petri Ihalainen, Jouko Peltonen, and Helge Lemmetyinen
Phys. Chem. Chem. Phys. **2010**, *12*, 12525.

III **Vectorial photoinduced electron transfer in multicomponent film systems of poly(3-hexylthiophene), porphyrin-fullerene dyad, and perylenetetracarboxidiimide**
Paola Vivo, Kimmo Kaunisto, Alexander S. Alekseev, Oili Pekkola, Antti Tolkki, Vladimir Chukharev, and Helge Lemmetyinen
Photochem. Photobiol. Sci. **2010**, *9*, 1212.

IV **Influence of Alq_3/Au cathode on stability and efficiency of a layered organic solar cell in air**
Paola Vivo, Johanna Jukola, Mikko Ojala, Vladimir Chukharev, and Helge Lemmetyinen
Sol. Energy Mater. Sol. Cells **2008**, *92*, 1416.

V Role of a phthalocyanine–fullerene dyad in multilayered organic solar cells

Paola Vivo, Mikko Ojala, Vladimir Chukharev, Alexander Efimov, and Helge Lemmetyinen

J. Photochem. Photobiol A **2009**, *203*, 125.

Author's contribution

Paola Vivo planned and carried out most of the experimental work and data analysis, and wrote all the publications listed above.

Abbreviations and symbols

A	acceptor
A	absorbance
AFM	atomic force microscopy
Alq_3	tris-8-hydroxy-quinolato aluminum
BCP	bathocuproine
C_{60}	buckminsterfullerene
CO_2	carbon dioxide
CS	charge-separated
CT	charge transfer
CuPc	copper phthalocyanine
D	donor
DHD6ee	porphyrin-fullerene dyad (see Figure 3.1)
DPV	differential pulse voltammetry
DSSC	dye-sensitized solar cells
ET	electron transfer
ETL	electron transporting layer
eV	electron volts; 1 eV = $1.60217646 \times 10^{-19}$ J
F	fullerene
FF	fill factor
$H_2Pc–C_{60}ee$	phthalocyanine-fullerene dyad (see Figure 3.1)
HOMO	Highest Occupied Molecular Orbital
HTL	hole transporting layer
IPCE	Incident Photon-to-Current Efficiency
IR	infrared
I_{SC}	short circuit current
ITO	indium tin oxide
I–V	current–voltage
LUMO	Lowest Unoccupied Molecular Orbital
MV^{2+}	methyl viologen
ODA	*n*-octadecylamine
OLEDs	organic light-emitting diodes
OPVs	organic photovoltaics
P	porphyrin
PC	photocurrent

PDI	N,*N'*-bis(2,5-di-*tert*-butylphenyl)-3,4:9,10-perylenebis(dicarboximide)
P–F, F–P	porphyrin-fullerene dyad, fullerene-porphyrin dyad
PHT	poly(3-hexylthiophene)
PTCDI	perylenetetracarboxidiimide
PV	photovoltage
S_0	ground state
S_1	first electronic excited singlet state
S_2	second electronic excited singlet state
TBD6a	porphyrin-fullerene dyad (see Figure 3.1)
TiO_2	titanium dioxide
toe	tonnes oil equivalent
TRMDC	time-resolved Maxwell displacement charge
TW	terawatt
U_{OC}	open-circuit voltage
UV	ultraviolet
V-79	violanthrone-79
V_{OX}	oxidation potential
V_{RED}	reduction potential
ZnPH4	zinc1(4),8(11),15(18),22(25)-tetrakis[3-(hydroxymethyl)phenoxy] phthalocyanine
Φ_E	external quantum yield of collected charges
Φ_I	internal quantum yield of collected charges
λ_{exc}	excitation wavelength
η	power conversion efficiency

1 Introduction

1.1 Motivation

The world demand for energy grows rapidly and continuously. In 2009, the total worldwide energy consumption was approximately 112×10^8 tonnes oil equivalent (toe),[1] which corresponds to an average power of roughly 15 terawatts (TW). This number is expected to rise of at least 10 TW by 2050, due to the growth of the population and of the world economy.[2] Most of the energy produced nowadays is derived from the combustion of fossil fuels, and the exponential energy demand is exhausting the resources alarmingly. As a consequence, the price of oil and gases is destined to rise remarkably and permanently. Moreover, the combustion of fossil fuels pollutes the environment with harmful substances, like carbon dioxide (CO_2) and other toxic gases, which significantly contribute to smog, global warming, acid rains, and so forth. To generate 10 TW of power by fossil fuels without affecting the environment, we would need to dispose of 25 billion metric tons of CO_2 produced annually. If the nuclear power would be the alternative source of energy, it would be required to build a new 1 gigawatt electric nuclear fission plant everyday for the next 50 years.[2] This catastrophic scenario clearly shows that there is no other clever option than to invest into environmentally clean energy resources. Different possibilities include hydroelectric resources, geothermal and wind-power systems, and solar energy. Among these, solar energy represents one of the most attractive technologies to meet the energy needs. Sunlight is free and unlimited. Moreover, solar energy is a clean, renewable, readily available, and ubiquitous energy source. However, at present the different routes to convert solar energy into electricity, fuel, and heat, are not yet competitive with fossil fuels in terms of costs, reliability, and performance. Every year the sun provides the earth surface with 120,000 TW·h of radiation.[3] Thus, it supplies in about 1 hour the energy needs for 1 year. In spite of such an enormous potential, in 2007 only 0.0087 TW of power were produced by photovoltaics. The huge gap between the present use of solar energy and its unexploited potential represents a great challenge in energy research. The photovoltaic industry is expected to grow at a rate of 15–20 % per year over the next decades.[4] To streamline and foster the adoption of photovoltaics on a large scale, the costs of the commercially available solar cells should be substantially reduced. To this aim, organic and polymeric photovoltaics appear to be a promising

and fascinating alternative to the silicon-based solar cells due to the lower costs of materials and processing, and to the ease of large manufacture. To overcome the main limitations of the existing organic photovoltaic devices, *i.e.*, the poor efficiency and stability, it is essential to deepen the understanding of the photoinduced interactions between different chromophores, which represent the essential constituents of light energy harvesting assemblies. Hence, the study of electron transfer (ET) in ultrathin film systems plays a key role in the design of efficient molecular devices for energy conversion applications.

1.2 Aims and outline of the Thesis

This Thesis aims to offer a contribution to the understanding of the photophysical processes taking place in organic thin films for photovoltaic applications. The heart of the studied multilayered structures is a highly oriented film of a donor–acceptor (D–A) pair, able to perform efficient primary ET.[5–17]

Recently, the ET in films of triads including an electron donor layer added to the D–A dyad was studied.[18–21] The primary ET takes place between the donor and the acceptor of the dyad, leading to a charge-separated (CS) state, and it is followed by a secondary ET, in which electrons are delivered by an additional donor layer (secondary donor) to the dyad.

However, not much information has been reported on the research of suitable secondary electron acceptors for the dyad, so to build more efficient multilayered systems of electron-donor, D–A pair, and electron-acceptor. The main contribution of this work is to investigate several *n*-type materials that can be used as secondary electron-acceptors. Moreover, multifunctional layers have been assembled in the same film structure, to enhance the separation of charges due to the multistep ET. Finally, learning to know the intra- and intermolecular photoinduced processes between the studied compounds enabled us to develop photovoltaic devices.

To achieve the mentioned aims, the following strategy was followed, which also reflects the structure of this Thesis:

1. Research of secondary electron-acceptors for the dyad[I,II]
2. Assembly of complex multifunctional configurations able to undergo multistep ET with enhanced final charge separation[III]
3. Testing the capability of some of the studied film structures to produce photocurrent in a three-electrode photoelectrochemical cell[I]

4. Optimizing of the organics|top-electrode junction so as to be able to use a metal cathode in the solar cells[IV]

5. Development of layered cells with a "donor|dyad|acceptor" layout, which proves the crucial role of the D–A pair in the devices.[V]

In points 3 and 5 the information from the ET studies (points 1 and 2) is used to build photovoltaic devices.

The numbering of the publications in the Thesis does not correspond to their chronological order.

2 Background

In this chapter, a brief introduction to organic photovoltaics (OPVs), starting from the fundamental mechanism of photoinduced charge transfer, is provided. The main features of organic solar cells are presented, together with an overview of the most common device architectures. Finally, widely used molecules for organic photovoltaics, classified according to their functional role in the cell, are introduced.

2.1 Photoinduced charge transfer

The photoinduced charge transfer (CT) between a donor and an acceptor molecule is a key mechanism for the natural photosynthesis[22] and for nearly all organic solar cell concepts.[23] This process takes place only under illumination, since it stems from the interaction between an excited state and a ground state. A donor (D) or acceptor (A) is excited by light, and thus promoted to its excited state. In the next step, an electron is transferred from D to A (electron transfer), or alternatively a hole transfers from excited A to D (hole transfer). The ET mechanism can be schematically described by the following consecutive steps:[23]

1: $D + A$	$\rightarrow$	$D^{*} + A$	(photoexcitation of D)
2: $D^{*} + A$	$\rightarrow$	$(D–A)^{*}$	(delocalization of the excitation)
3: $(D–A)^{*}$	$\rightarrow$	$(D^{\delta+}–A^{\delta-})^{*}$	(polarization of the excitation)
4: $(D^{\delta+}–A^{\delta-})^{*}$	$\rightarrow$	$(D^{\bullet+}–A^{\bullet-})$	(formation of ion radical pair)
5: $(D^{\bullet+}–A^{\bullet-})$	$\rightarrow$	$D^{\bullet+} + A^{\bullet-}$	(final charge separation)

After the final CS state is obtained, charges can recombine back to the ground state. In the ET processes, D and A can be either two separate molecules, or two moieties of the same molecule. The first case and second case are usually referred to as intermolecular and intramolecular, respectively. Molecular dyads, in which photoactive donors are covalently linked to electron-acceptor moieities, are exceptional examples of efficient intramolecular ET systems.[5–17]

Several requirements have to be fulfilled in order for the ET to take place. Since the distance between the two molecules involved in the ET process must be short, a significant coupling of the electronic wave functions of D and A is required.[24,25] In addition, the orientation between the molecules plays also a great role.[26] Finally, the relative position of the energy levels of the molecules involved in the ET is crucial.

The charge separation can take place only if the offset between the Lowest Unoccupied Molecular Orbital (LUMO) of D and A is large enough to overcome the coulombic attraction between the charges.[23]

A more detailed description of the energetics and kinetics of the photoinduced CT reactions is presented in the theories of Marcus and Jortner.[27–29]

Fullerene and its derivatives are widely used as electron acceptors in ET reactions, due to their high electron affinity resulting from an energetically deep LUMO level of –4.3 electron volts (eV) *vs.* vacuum.[30] The ET processes involving fullerenes play an important role in the field of organic optoelectronics, including photodiodes, photovoltaic cells, and phototransistors.

2.2 From inorganic to organic solar cells

Solar cells convert sunlight into electricity through the so-called photovoltaic effect, discovered by Edmond Becquerel in 1939.[31] He studied the effect of light in electrolytic cells, observing the generation of voltage in a material upon electromagnetic excitation. This is the basic physical principle of all the photovoltaic devices.

The first solid-state solar cell is credited to Charles Fritts in 1883, who used a Se semiconductor as absorbing layer with a rectifying metal contact.[32] The biggest impact on the development of the solar cells technology was however given in 1953 by the accidental discovery at Bell Laboratories.[33] Chapin, Fuller, and Pearson developed a cell based on a Si *p-n* junction with approximately 6 % power conversion efficiency. The skeleton of most the modern photovoltaics still resembles this first Si-based cell, although a lot of improvements have been achieved in terms of efficiency and stability of the devices. The highest efficiency achieved with single crystal Si cells is 24.7 %.[34] With a tandem cell approach, consisting in stacking several devices in series (tandem cell configuration) so as to capture as many incident photons as possible, efficiency has been increased up to 40.8 %.[35] Recently, even higher efficiencies have been achieved, 41.1 %, and 42.8 %, at the Fraunhofer Institute for Solar Energy Systems (ISE) in Freibrug[36] and at the University of Delaware,[37] respectively. These world-record efficiencies are related to very complex platforms based on crystalline Si and/or other inorganic semiconductors.

The solar cell industry is currently still dominated by this so-called first-generation solar cells based on Si wafers, which cover nearly 90 % of the market.[38] It is however important to underline that the efficiency of most of the

commercialized Si-based solar cells is between 14 % and 19 %,[39] which is much lower than the highest values previously reported. In fact, efficiency improvements often result in additional costs, and for the mass production it is mandatory to reduce the cost-to-performance ratio as much as possible.

In spite of the promising efficiencies reachable with the conventional inorganic photovoltaics, the bottleneck in the routine use of such technology as a household energy source is the high cost. The current price for solar energy is roughly 0.25–0.65 $/kWh, which is approximately 5 times higher than electricity obtained from fossil fuels.[38] The reason lies in the very expensive materials and processing techniques needed to build up the solar modules. Attempts to diminish costs include the reduction of the amount of Si (thinner Si wafers), or the replacement of Si with other suitable materials like cadmium telluride (CdTe) and copper indium gallium selenide (CIGS).[38] These thin-film based solar cells belong to the second-generation of photovoltaics, characterized by lower production costs than the first-generation devices, but also by lower efficiencies. Moreover, the thin-film solar cells are flexible, and can lead to innovations such as solar shingles and solar panels that can be rolled out onto any surface. The efficiencies of this second-generation solar cells typically lie in the range of 9-12 %,[40] or higher (around 30 %) with tandem cell approach.[41]

In the last three decades, at the cutting edge of the solar technology are the third-generation solar cells, including dye-sensitized solar cells (DSSC), organic small molecule and polymeric solar cells, nanocrystal solar cells. These devices are starting to emerge on the market, but are still in the research stage nevertheless.

The basic difference between the third-generation of solar cells and the previous generations (first and second) is that they do not rely on a traditional *p-n* junction to separate the photogenerated charge carriers.

The DSSC were discovered by O'Regan and Grätzel in 1991 and for this reason they are also known as Grätzel cells. They are composed of a nanoporous layer of titanium dioxide (TiO_2), covered with a molecular dye. TiO_2 is placed in contact with a redox electrolyte solution or an organic hole conductor. The photoexcitation of the dye results in the injection of an electron in the conduction band of the oxide. The electrolyte is usually an organic solvent containing a redox system, typically the iodide/triiodide couple. The regeneration of the dye takes place through electron donation from the electrolyte.[42,43] Nowadays, DSSC have reached efficiencies over 11 %,[44] and for this reason they are currently the most promising alternative to the Si-based solar cells. However, research is continuously aiming to improve

efficiency, stability, and scalability of the devices. In the latest years, the use of solvent-free electrolytes has led to striking improvements in this direction.[45]

OPVs have been developed for more than 30 years, with a peak in the research activity during the last decade.[46–49] In spite of their still not competitive efficiencies, which have reached the highest values of 7.4 %[50] and 7.9 %[51], organic solar cells represent an attractive technology in the solar energy research. Their potential advantages when compared to the Si-based cells are the light weight, the flexible shape, the versatile device fabrication schemes, the low cost on large-scale industrial production, the integrability of plastic devices into other products such as textiles and consumption goods, and the continuous tunability of optical (energy) band gaps of materials via molecular design, synthesis, and processing.[4] Several consumer electronics based on the organic photovoltaic technology are emerging on the market, like portable chargers, wearable electronics, solar umbrellas, just to mention a few of them.[52]

The tandem approach described before can offer a strategy to increase the efficiency of the OPVs. Kim *et al.* reported about a high efficiency tandem device with a 38 % performance improvement *vs.* the best single device.[53] This approach allows overcoming the main intrinsic limitations of organic materials used in OPVs, which is their rather poor charge carrier mobility, and the narrow spectral overlap of the absorption spectra of the organics with the solar spectrum.[54]

While the efficiencies of organic solar cells are steadily improving, a limited set of relevant data is available on the lifetime performance and the degradation of such devices.[55–59] The optimization of the stability is an essential step in the OPVs research. The achievement of long-term durability by storing the devices in ambient air, with no special requirements and preferably without the need for encapsulation, is crucial to reduce the costs of the technology. At the present, the longest reported lifetime for encapsulated OPVs is over one year in outdoor conditions.[55]

2.3 Basic working principles of organic photovoltaics

Organic semiconductors can transport electric current and absorb light in the ultraviolet (UV)-visible part of the solar spectrum due to their delocalized π conjugation. They present several differences with the conventional inorganic semiconducting materials. The charge mobility of organic materials is several orders of magnitude lower than that of inorganic compounds. However, the low mobilities in organic semiconductors are partly balanced by their relatively strong absorption coefficients (typically $\geq 10^5$ cm^{-1}), which allow high absorption in ≤ 100

nm thick devices. Another main difference between organic and inorganic semiconductors is that in inorganic materials the light absorption (primary photoexcitation) generates free charges, separated at the junction. In the case of organic materials, the results of the photoexcitation are electron-hole pairs called excitons. The excitons are neutral excited states, with typical binding energy from 0.05 to >1 eV. The exciton diffusion length is typically 5–15 nm, which corresponds to the path over which they can diffuse before decaying either radiatively or nonradiatively to the ground state (lifetime from picoseconds to nanoseconds[60]).

As a consequence of the mentioned differences in the conduction taking place in the amorphous and disordered organic materials and the inorganic ones, the whole photoconversion mechanism in inorganic and organic photovoltaics is radically different. Organic solar cells operate in a drift mode, while the functioning of crystalline silicon based devices is based on a diffusive mode.

The process of conversion of light into electricity by means of organic solar cells takes place through intermediate charge separated states called geminate pairs, which are fundamental intermediates in the photoconversion process. They need strong electric fields to be applied in order to be dissociated into free charge carriers.[61]

The whole process is schematically described by the following consecutive steps: (i) *photon absorption* with the formation of an excited state, *i.e.*, the exciton (electron–hole pair); (ii) *exciton migration* to a diffusion zone, where the (iii) *charge separation* takes place; (iv) *charge transport* to the respective electrodes, and (v) *collection* of the charges by the electrodes.[4,61] A schematic view of how an organic solar cell works is reported in Figure 2.1. The current produced by a photovoltaic cell corresponds to the number of generated charges which are collected at the electrodes. This number depends on the fraction of absorbed photons, the fraction of excitons that are dissociated, and that of the separated charges reaching the electrodes.[61]

In step (i), a fundamental requirement is that the optical gap of the materials, which is the difference between the Highest Occupied Molecular Orbital (HOMO) and LUMO, should be equal or close to the incident photon energy. Once the exciton is photogenerated, its diffusion (step ii) to a remote site takes place via intrachain or interchain energy transfer or *hopping*. The separation of the coulombically bound charge pairs (geminate pairs) into free charge carriers (step iii) requires a process to be introduced, since the built-in electric fields of organic

semiconductors are usually not high enough to dissociate the geminate pairs directly. One possibility is that the separation occurs at a

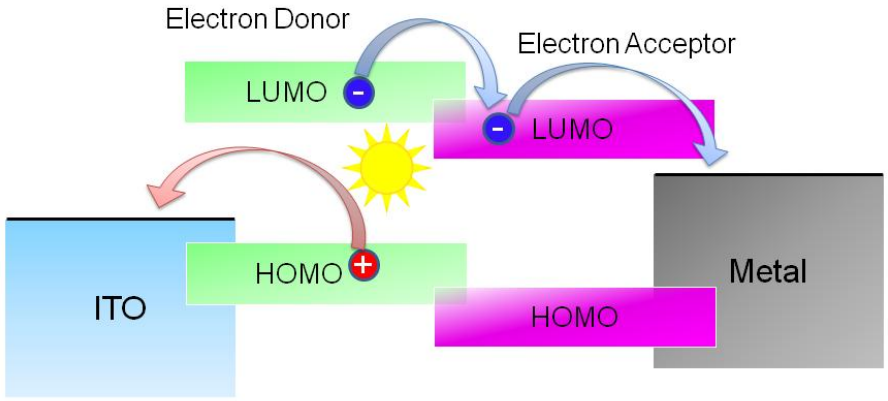

Figure 2.1 *Simplified picture of the basic processes occurring in organic solar cells.*

donor–acceptor interface, due to the significant driving force generated by the energy difference between the donor–acceptor frontier orbitals (*i.e.*, HOMO and LUMO). Once free electrons and holes are generated, they diffuse (step iv) and are collected (step v) at the low work function and high work function electrodes, respectively. Typically, Al is used as low work function electrode (acting as cathode of the cell), and indium tin oxide (ITO) as high work function electrode (acting as anode).

2.4 Organic solar cell architectures

The differences between the existing organic solar cell architectures lie mainly in the exciton dissociation process, which can occur at different locations within the photoactive layer. In this section, the most widely investigated device layouts will be described, *i.e.*, single layer, bilayer and multilayer heterojunction, and bulk heterojunction solar cells.

2.4.1 Single layer

The single layer solar cells are the earliest examples of OPVs. They are based on a single organic layer (typically thermally evaporated), sandwiched between two metal electrodes with different work functions.[4,61] The charge separation requires a Schottky barrier at one of the organic|electrode interfaces. The photovoltaic

parameters, and thus the efficiencies, of single layer solar cells are strongly influenced by the nature of the electrodes. Highest reported efficiency values reach 0.3 % for heavily doped conjugated materials.[46] Such devices are very inefficient, due to the small exciton diffusion length of most organic materials, which limits the photogeneration to take place only in a thin layer near the interface. In these devices, the generated electric field is seldom sufficient to dissociate the photogenerated excitons. Moreover, electrons tend to recombine with the holes rather than to reach the electrode. The problems of the single layer layout can be partly overcome with the introduction of multilayer organic photovoltaics.

2.4.2 Bilayer heterojunction

In 1986, Tang reported a breakthrough in the performance of organic solar cells, achieving a nearly 1 % efficiency under simulated solar illumination.[62] The concept of Tang's cell is a bilayer device, where a donor and an acceptor material are stacked together to form an organic heterojunction (Figure 2.2a). In such a kind of donor|acceptor solar cell, the charge separation takes place at the planar interface between donor and acceptor. A proper alignment of the energy levels between the donor and acceptor layers is fundamental for efficient exciton dissociation; a large energy difference between them makes the exciton dissociation possible. The bilayer is sandwiched between two electrodes whose work functions match the donor HOMO and acceptor LUMO, so as to enable charge extraction at the respective electrodes. The photoinduced electron transfer is a key mechanism in this kind of cells. The photon absorption in the donor excites an electron from the HOMO to LUMO of the donor, which is followed by ET from the donor LUMO to the acceptor LUMO.

A big advantage of bilayers compared to single layer cells is the monomolecular charge transport after the exciton dissociation. Electrons can travel through the *n*-type acceptor (electron transporting layer, ETL), and holes through the *p*-type donor material (hole transporting layer, HTL). This produces an efficient separation of the charges, which greatly reduces the possibility of charge recombination.[61]

Since the first double-layer structured solar cell introduced by Tang, different materials and configurations have been proposed in order to improve the cell performance.[63–68] Xue *et al.* have published a 4.2 % efficiency double-heterostructure organic photovoltaic cell,[65] and one year later they reached 5 % efficiency with a hybrid planar-mixed molecular heterojunction photovoltaic cell.[66]

More recently, even an efficiency value of 5.58 % was obtained for a rubrene-doped bilayer heterojunction device by Chan *et al.*[68]

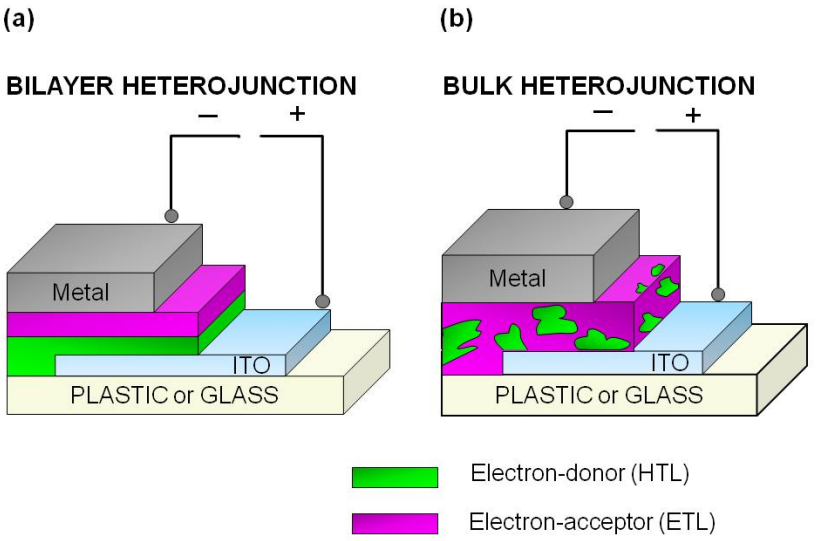

Figure 2.2 *Schematic configuration of a bilayer heterojunction (a) and bulk heterojunction (b) solar cell.*

The concept of bilayer solar cell can be extended, and several heterojunctions can be introduced in a cell, resulting in the so-called multilayered solar cells, where additional layers are added to the donor and acceptor. Such layers do not always contribute to the photocurrent generation, but can have a different function in the cell, like in the case of the buffer layers, which are generally introduced for better hole (electron) accepting/transporting/blocking properties (see Section 2.8).
This Thesis will focus on the multilayered solar cells, which will be described in publications II, IV, and V.

2.4.3 Bulk heterojunction

While in the bilayer heterojunction donor and acceptor are completely separated one from the other, in the bulk heterojunction concept both phases are intimately mixed to form an interpenetrating network (Figure 2.2b). As a result, the active surface area of the interface increases, and the excitons can dissociate wherever

they are created within the bulk.[61,69–72] The two-dimensional interface of the bilayer approach is here exchanged by a three-dimensional interpenetrating network.

Bulk heterojunction solar cells were reported the first time in 1995 with efficiency below 1 %.[69] After a few years the number of publications in this field grew exponentially. Currently, the highest reported efficiency is 7.9 %,[51] and several other examples of cells with efficiencies between 4 and 6 % have been published.[53,73–76]

The high interest in bulk heterojunction solar cells arises from their reasonably high efficiency, combined with the cheap and easy device fabrication technology. In fact, they can be prepared by solution processing techniques, such as spin-coating, doctor blading,[77] screen printing,[78] inkjet printing,[79] and spray coating.[80] The printing technology is especially considered very attractive since it enables roll-to-roll fabrication of flexible devices with large area.

However, even if the preparation of bulk heterojunction photovoltaics is rather simple, their mechanisms and operation principles are complex and not completely clarified yet.

2.5 Electron–donor materials

2.5.1 Porphyrins and phthalocyanines

Porphyrins are pigments that can either occur in nature or be synthetically prepared. They have many applications, including biological[81,82] and artificial electron transfer systems,[10,83–85] as well as catalytic substrate oxidation,[86,87] just to mention a few of them.

Porphyrins contain a fundamental skeleton of four pyrrole nuclei connected at their α-carbons via methine bridges to form a planar macrocyclic structure.[88] Their basic structural unit is named porphine, and it is showed in Figure 2.3a. Due to their high conjugation, porphyrins show intense absorption in the visible region, and therefore are deeply colored. The absorption spectra of porphyrins are characterized by a strong band at approximately 410–450 nm, which corresponds to the Soret-band.[81] Moreover, four weaker bands in the wavelength range 450–750 nm, the Q-bands, can be identified.

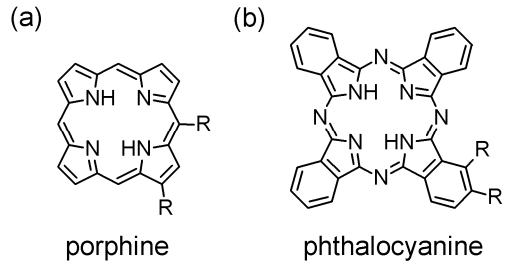

Figure 2.3 *Molecular structures of porphine (a) and phthalocyanine (b). In the structures, R marks the position for the substitutions described in the text.*

Phthalocyanines are structural analogues of porphyrins. The difference between them is that in phthalocyanines the four pyrrole units are benzo fused to form isoindoles, and connected via aza bridges (Figure 2.3b). An attractive feature of both porphyrins and phthalocyanines is their great versatility, since the two hydrogen atoms of the central cavity can be replaced by over 70 central metals. Moreover, different moieties can be substituted in the axial position or at the periphery of the macrocycle, giving rise to a variety of compounds with different physical properties.

Phthalocyanines represent a class of materials with exceptional electronic and optical properties arising from their electronic delocalization.[89] They are widely used as industrial dyes and as catalysts. In the last decades, these compounds have been receiving an increasing interest as electron-donor and antennae materials in energy conversion systems, mainly coupled with fullerene.[63,90–99] In their absorption spectra, phthalocyanines have a Soret-band around 320–360 nm and an intense Q-bands in the visible region, with absorption maxima around 620–700 nm. This explains their characteristic dark green-blue color.[95] Such a feature makes them more attractive chromophores for photovoltaics than porphyrins, because of the better matching of their absorption spectrum with that of the sun.

2.5.2 Polythiophenes

Polythiophenes (Figure 2.4) are the most common conducting polymers used in organic solar cell applications. Their intrinsic conductivity arises from the extended and delocalized π–conjugation.[100] Conducting polymers usually contain simple heteroatoms like N and S (in addition to the usual C and H). The conductivity is achieved by chemical or electrochemical oxidations or reactions, or by introducing a certain number of dopants, *i.e.*, anionic or cationic species. In other words, the

polymer backbone needs to be oxidized or reduced to introduce charge carriers so to observe conductivity. In organic solar cells, the conjugated polymers become charged as a consequence of a photoinduced ET reaction.

Poly(3-hexylthiophene) (**PHT**) is a promising and widely studied electron-donor material, due to its excellent charge transport properties. Moreover, it absorbs in a wide part of the visible region, between 400 and 650 nm,[101] with an absorption edge around 650 nm, close to the sun's maximum photon flux (650–700 nm).

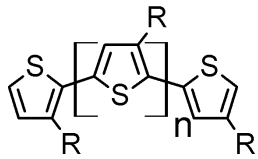

Figure 2.4 *Chemical structure of polythiophenes.*

Blends of **PHT** and fullerene (or fullerene derivatives) are widely studied configurations for organic photovoltaics, giving rise to the most promising efficiencies. Performance depends strongly on the material properties and processing conditions (*e.g.*, thermal annealing). The molecular nanostructure of **PHT**, related to the self-organizing properties of the polymer, has a relevant influence on its optoelectronic properties and on the device performance. However, a clear relationship between these parameters has not yet been clarified.[102]

2.6 Electron–acceptor materials

2.6.1 Fullerenes

Fullerenes are a class of molecules in which the atoms are arranged in closed shells with generic formula C_n (n= number of atoms in the shell, varying from 20 to 80). Among the whole family of hollow cage carbon clusters, the most abundant and widely studied are C_{60} and C_{70}.

Fullerenes were discovered in 1985 by Kroto, Curl, and Smalley,[103] who received Nobel Prize in Chemistry for 1996. However, the major breakthrough in the development of the fullerene chemistry was given by Kratschmer *et al.*[104] who proposed a very simple way to synthesize it. After this discovery, fullerenes research developed rapidly and widely. The photochemical and photophysical properties of fullerenes and derivatives have been intensively studied for a few decades, because of their fascinating optical and redox properties.[10,105–107]

Ultrathin electron-acceptor layers of fullerenes are used in organic solar cells, especially the fullerenes derivative phenyl-C_n-butyric-acid-methyl-ester ([n]PCBM), probably the most efficient class of electron acceptors among those available for organic solar cells.

We will hereby focus only on C_{60}, since it is the compound used in this Thesis, and in the following we will refer to it as fullerene. C_{60} is a molecule consisting of 60 carbon atoms, arranged as 12 pentagons and 20 hexagons. The molecule has the shape of a football, *i.e.*, of truncated icosahedrons (Figure 2.5).

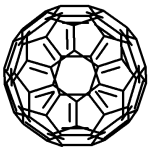

Figure 2.5 *Molecular structure of C_{60}.*

Fullerene is an electronegative molecule, able to accept up to six electrons in solution, and it is a good electron-acceptor compared to other organic molecules.

One of the most remarkable properties of C_{60} as an enabler for artificial photosynthetic systems is that it allows efficient and fast photoinduced charge separation, together with a slow charge recombination in the dark.[108]

C_{60} absorption is intense in the UV region of the spectrum (below 300 nm), while only a moderate absorption is shown in the visible.

2.6.2 Perylenes

Perylene is a planar aromatic compound consisting of two naphthalene molecules connected by a carbon-carbon bond at the 1 and 8 positions. All of the carbon atoms in perylene have the sp^2 hybridization. Perylene dyes present good solubility, absorption, and emission properties that can be efficiently tuned by functionalisation with hydrophobic, hydrophilic, electron-donating or electron-withdrawing groups.[109]

Due to the strong π–π interaction between fused aromatic ring structures, the perylene structure tends to form assemblies, and such π–stacking is expected to facilitate energy or charge transport.[110]

Perylene and its derivatives show interesting electrical and optical properties, which make them exceptional candidates for several applications, such as organic semiconductors, photoconductors, photoreceptors and laser materials.[111]

In the Thesis, two substituted perylenedicarboximides were used.[I–III,V] Perylenedicarboximide derivatives show remarkable electrical, chemical, and photochemical stability.[111] Moreover, this class of dyes has high absorption coefficients in the visible region ($\varepsilon \approx 10^5$ L mol^{-1} cm^{-1}),[112] and fluorescence quantum yields close to unity.[113]

These molecules have been used as building blocks for different types of devices, including (but not limited to) molecular switches,[113] organic light-emitting diodes (OLEDs),[114,115] photovoltaic cells (as light-harvesting antennae),[116,117] wires,[118] and logic gates.[119] Perylene dicarboximide derivatives have been also adopted as photoconducting materials in xerography,[120–122] optical communication devices,[123,124] and as photoinduced electron transport materials.[125]

2.7 Donor–Acceptor (D–A) pairs

In the photosynthesis, green plants convert the light energy into chemical energy. Molecular dyads, in which photoactive donors are covalently linked to electron acceptor moieties, have been synthesized as light harvesting assemblies, to mimic the photoinduced ET process of natural photosynthesis.[2,10,126–132] These molecular D–A pairs are interesting examples of photoinduced ET systems.[5,6,10,13–15] Typically, they are characterized by long lifetimes of the CS state and efficient geminate pair dissociation, which streamline the collection of the charges at corresponding electrodes, thus generating photocurrent. Many examples of D–A systems can be found in literature, as suitable candidates for OPVs.[II,III,V,92,133–142]

Widely studied dyads typically contain porphyrin derivatives as donors, and C_{60} as acceptor. In this work, a covalently-linked porphyrin-fullerene dyad, capable of undergoing efficient ET from porphyrin to fullerene yielding the porphyrin cation and fullerene anion moieties, was mainly used.[I–III] The porphyrin moiety of the dyad ensures efficient absorption in the visible region of the spectrum. The ET in covalently-linked porphyrin-fullerene dyads has been studied in solution,[7,84,143–148] and in films.[19–21,149,150,I–III] The most common deposition techniques for the fabrication of dyad monolayers for oriented ET systems are the Langmuir–Blodgett method and the self-assembly. The energy levels of fullerene moieties lie below those of porphyrin.[9,148] This results in energy transfer from the porphyrin singlet excited state to fullerene, which can compete with the ET, and in the achievement of the charge separation between the two moieties through the formation of an emittive exciplex intermediate.[7]

Phthalocyanine chromophores have some advantages over the porphyrin ones, since they absorb the light in a wider spectral region. Phthalocyanine-fullerene dyads are potentially good D–A pairs for organic photovoltaics, due to the exceptional electronic and optical properties of the phthalocyanine and fullerene moieties. Nevertheless, not many studies about such dyads are reported in literature, because the synthesis of the compounds is quite a challenging task. Particularly, the introduction of phthalocyanine-fullerene dyads in organic solar cells is described only in a few works.[136,138,V]

In [V], a phthalocyanine-fullerene dyad has been used for solar cell applications. Its photophysical properties had been thoroughly studied both in solution[151,152] and in solid films.[98] These studies reveal that efficient intramolecular ET takes place from phthalocyanine to fullerene, which leads to the formation of a CS state with nanosecond and microsecond lifetimes in solution and in solid films, respectively.

2.8 Buffer layers

The charge carrier transport at the interface between the organic materials and the electrodes is difficult. In order to improve it, a widely used solution is to introduce a thin interlayer, called buffer layer, which has several functions. Among them, it adjusts the electronic behaviour of adjacent materials,[153] it protects the organics from the diffusion of the electrode, and obstructs the permeation of oxygen and/or water molecules.

The buffer layers have usually specific blocking and/or transport properties. Most of the published studies refer to the interface between ITO and organics, where a thin layer of poly(ethylene dioxythiophene) doped with polystyrene sulfonic acid (PEDOT:PSS) has been widely used to improve the charge transportation. PEDOT:PSS is a good HTL material, and when spin-coated on ITO, it smoothes its surface and enhances the adhesion of the organics onto ITO. The main drawback of PEDOT:PSS is its degradation under UV illumination. Moreover, due to the highly hygroscopic nature of PEDOT:PSS,[154] it introduces water into the organic films. The thermal treatments post deposition (annealing) in air are generally unstable due to the fast water uptake. For example, the conductivity of PEDOT:PSS is reduced by roughly one order of magnitude when measured in air.[154,155] Hence, it is not convenient to use PEDOT:PSS in open air experiments, but only in inert atmosphere (*e.g.*, glove-box). Since all the solar cells presented in this study were fabricated and measured in air, we did not introduce a

PEDOT:PSS layer on the ITO surface, but we deposited the organic materials directly on top of ITO.

The interface between organics and the metal electrode has also been investigated. The introduction of a buffer layer onto the organics prior the metal evaporation into bulk heterojunction or layered cells has been reported in several works.[156–163]

The electron collection via direct contact between the electron-acceptor layer (typically C_{60}) and the metal cathode is not efficient.[164] The introduction of an ETL between the organics and the metal is essential for an efficient electron collection. The ETL acts as a buffer layer, protecting the top organic layer from the damage caused by the metal deposition. The thickness of the buffer layer strongly affects the cell performance, and it requires optimization. Usually the ideal thickness is only a few nanometers.

Several materials have been proposed as buffer layers to optimize the organics|metal electrode junction, with bathocuproine (BCP), lithium fluoride (LiF), and tris-8-hydroxy-quinolato aluminum (**Alq_3**) being the most widely adopted. Peumans and Forrest demonstrated how to improve the power conversion efficiency of the copper phthalocyanine (**CuPc**)|fullerene (**C_{60}**) double heterostructure cell through the introduction of a BCP layer, which acts as exciton blocking and electron transporting layer.[64] However, BCP-based cells show stability problems due to the rapid BCP crystallization, especially in the presence of moisture.[157] A potential solution to such problem relies on the use of **Alq_3** instead of BCP. It was tested that by replacing BCP with **Alq_3** between **C_{60}** and Al cathode, the lifetime of the conventional **CuPc|C_{60}** cell could be extended from less than 1 h to about 60 h.[156] In [IV], the introduction of **Alq_3** into an Au-cathode solar cell is discussed in terms of influence on the efficiency and lifetime of the device.

3 Materials and methods

This chapter presents the compounds studied in the Thesis, and shortly introduces to the film preparation and characterization techniques adopted in the study. A full description of the experimental techniques is supplied in the publications.[I–V]

3.1 Compounds

The molecular structures of all the compounds investigated in this work are presented in Figure 3.1, where the molecules are grouped according to the characteristics of being electron donors (HTL materials), D–A pairs, electron acceptors (ETL materials), or buffer layers.

The D–A pairs (**DHD6ee**,[165] **TBD6a**,[165] **H_2Pc–C_{60}ee**[151]) and the phthalocyanine derivative (**ZnPH4**[151]) were synthesized at the Department of Chemistry and Bioengineering, Tampere University of Technology. All other compounds were commercially available and used without further purification.

From now on, the acronyms **P–F** or **F–P** will be used for the porphyrin-fullerene dyads (**DHD6ee** or **TBD6a**) to indicate the location of the porphyrin (**P**) and fullerene (**F**) moieties of the dyad in the films relative to other molecular layers.

CuPc and fullerene **C_{60}** are the best-known donor and acceptor for organic small-molecules based solar cells. In paper IV, they have been used as efficient HTL|ETL pair in Au-cathode cells.

Porphyrin-fullerene and phthalocyanine-fullerene dyads represent the essential core of the multilayered cells based on photoinduced ET. In the dyads, an efficient primary ET takes place.[I–III,V] The charge separation distance can be increased, and the lifetime of the CS state prolonged if the D–A pair monolayers are coupled with films of secondary donors and/or acceptors. A multistep ET can take place in one defined direction in multilayered systems, where each layer is responsible for a specific function.

Highly regioregular (90–93 %) poly(3-hexylthiophene) (**PHT**) was used as HTL material in [I,III,V]. Its electron-donating characteristics are well known, since **PHT** is the most widely used *p*-type polymer in organic solar cells. Introduction of **PHT** has a key role in the performance of the solar cells, due to its broad absorption in the central part of the visible spectrum (absorption maximum at 540 nm).

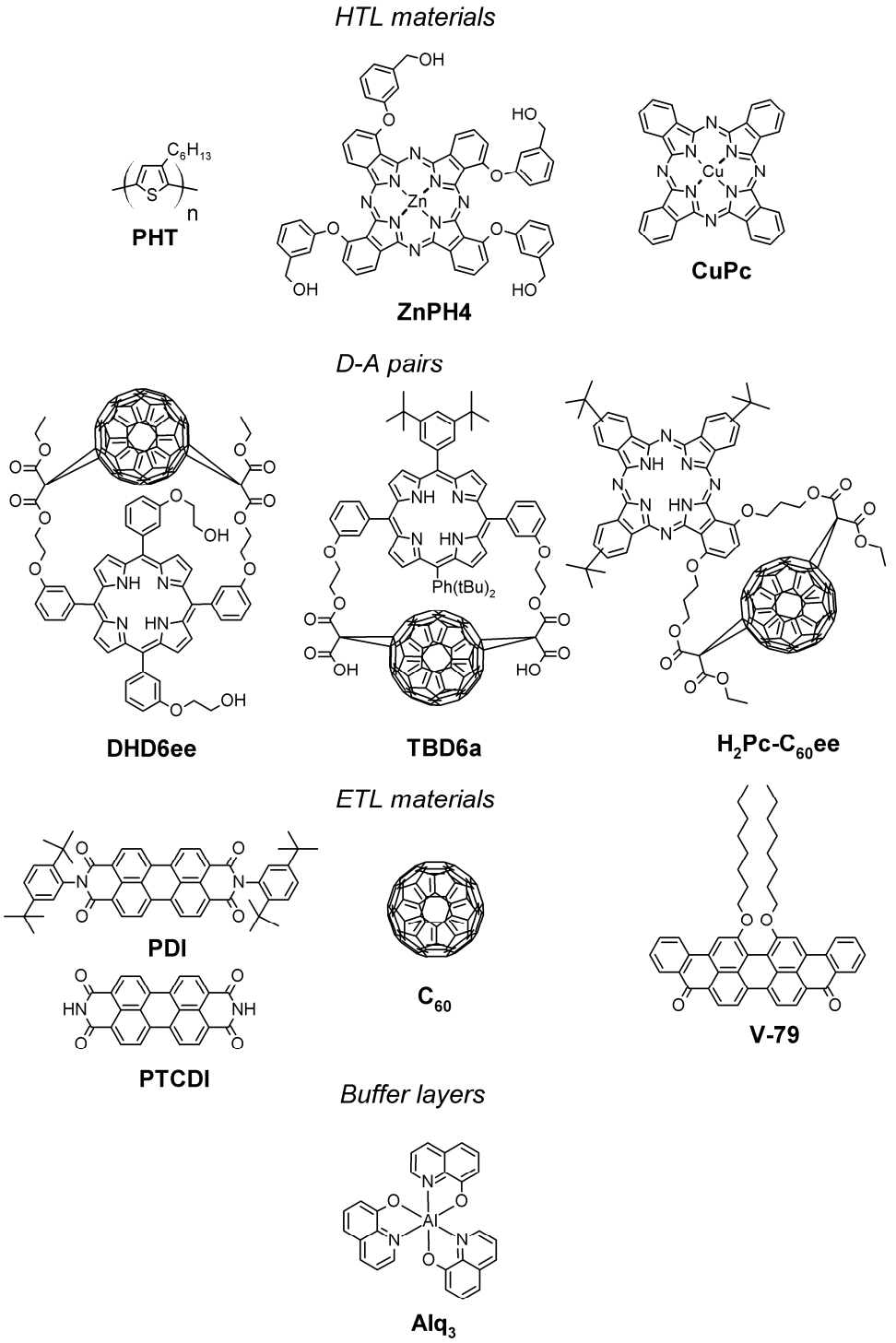

Figure 3.1 *Chemical structures and acronyms of the compounds used in the Thesis.*

The role of **PHT** as secondary donor for the porphyrin cation of **P–F** [I,III] has been already demonstrated earlier.[18,166] Secondary electron-donation takes place as well from **PHT** to **H_2Pc–C_{60}ee**[V]. The addition of **PHT** to the film structures is responsible for a significant increase in the amplitude and lifetime of both electrical and optical signals.[III] **ZnPH4** was also used as HTL in the photovoltaic devices of paper I, based on the promising results of the **PHT**|**ZnPH4** heterojunction present in literature.[20] In [I], violanthrone-79 (**V–79**) and N,*N*'-bis(2,5-di-*tert*-butylphenyl)-3,4:9,10-perylenebis(dicarboximide) (**PDI**) were exploited as ETL materials with respect to **PHT** and to the photoinduced fullerene anion of **P–F**. In [II], perylenetetracarboxidiimide (**PTCDI**) was studied as ETL material with several advantages compared to **PDI**.[I]

For all the photovoltaic devices with a metal top-electrode, a thin layer of **Alq_3** has been used as buffer layer, to protect the active layers from the evaporation of the cathode.[II,IV,V]

3.2 Film deposition methods

The films studied in this work have been prepared by means of several different methods. Among these, the Langmuir–Blodgett and Langmuir–Schäfer techniques enable obtaining highly oriented ultrathin organic films, while spin-coating and thermal evaporation give rise to unoriented layers.

3.2.1 Langmuir–Blodgett and Langmuir–Schäfer techniques

The Langmuir–Blodgett (LB) technology allows building highly organized nanometer-scale thickness molecular arrays where the moieties can be oriented in specific directions and be positioned at desired locations. It involves the vertical movement of a solid substrate through the monolayer/air interface.[167] In the most common case, the substrate is hydrophilic and the first monolayer is transferred as the substrate is raised from the water. Subsequently, following monolayers are deposited on each traversal of the monolayer/air interface. In this deposition, which is called Y-type, the monolayers are stacked up in a head-to-head and tail-to-tail pattern. There exist also two additional deposition modes, X-type and Z-type, when the monolayer transfers on the downstroke only or on the upstroke only, respectively.

The LB films are prepared by spreading a solution of the material under investigation onto a liquid surface (subphase) in a Langmuir trough. After the

solvent evaporates, the monomolecular layer so produced is compressed until a quasi-solid one molecule thick layer is formed. The next step is to transfer the monolayer from the subphase, by dipping and raising a suitable substrate through the compact monolayer. A schematic view of the LB deposition is depicted in Figure 3.2. Before the actual film deposition, isotherms must be recorded in order to establish the optimal dipping conditions. These are obtained by compressing the monolayer at constant rate and recording the surface pressure *vs.* the mean molecular area. The compression system is coupled to a microbalance which continuously monitors the surface pressure by means of a sensor in the subphase. The choice of the best surface pressure for the LB deposition depends on the nature of the monolayer. Generally, organic thin films are transferred at the surface pressure corresponding to the solid phase, which is 20–40 mN m^{-1} in the case of fatty acids. During the deposition the pressure is kept constant by moving the trough barriers to reduce the area available to the amphiphiles. The deposition of a monolayer takes place during immersion of the substrate into the water surface if the substrate has a hydrophobic surface. In this case the hydrophobic alkyl chains will interact with the surface, and the substrate will be hydrophilized. If the substrate has originally hydrophilic character, the monolayer will be transferred during the emersion. The hydrophilic headgroups are turned towards the hydrophilic surface of the substrate, and the resulting LB film will be hydrophobic.

The substrate is repeatedly dipped through the subphase and under proper conditions it is possible to transfer one monolayer for each excursion of the substrate through the water surface.

An alternative method to the vertical dipping process (LB) to transfer a floating monolayer to a solid substrate or to build multilayered film systems is the Langmuir–Schäfer (LS) technique. It consists in lowering a hydrophobic substrate horizontally so that it contacts the hydrophobic ends of the floating monolayer, and then lifting away the plate with the deposited film (Figure 3.2). This technique is very useful with very rigid monolayers.

In paper I, all the studied films were prepared by the LB technique, except for the photocurrent measurements where spin-coated **PHT** and **ZnPH4** were used. For most of the LB films, an octadecylamine (ODA) matrix had to be used to ensure a transfer ratio close to the unity. Based on the main idea that the introduction of ODA, which is an insulator, could decrease the conductivity of the films, the latest research in our laboratory aimed to build oriented molecular film structures constituted by active molecules alone, and to study the ET in such film systems.[II,III] This achievement was possible by replacing the LB technique with the LS

technique. In papers II and III, the **P–F** and **PHT** films were deposited by the LS method as 100 mol % films.

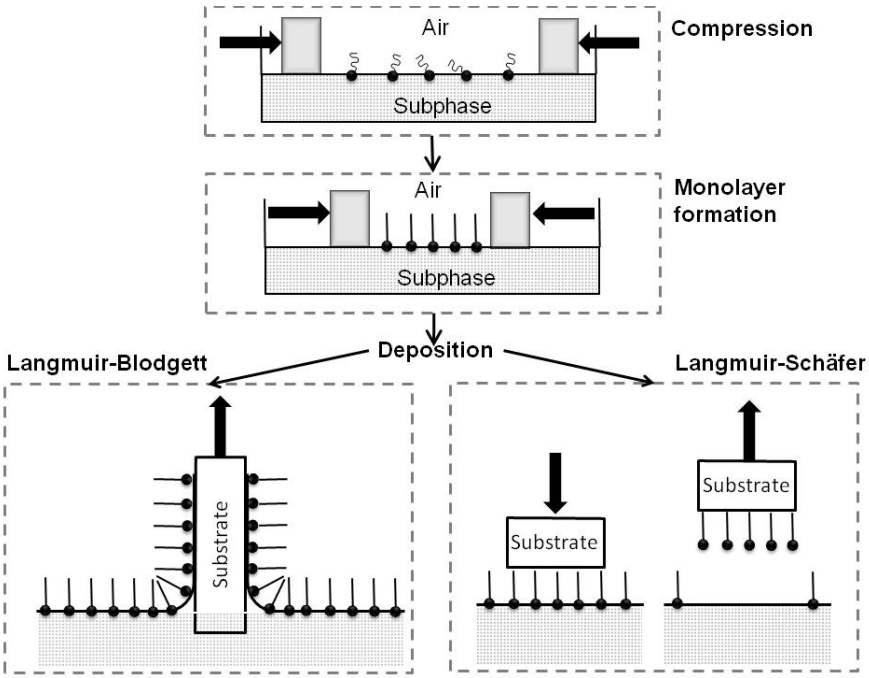

Figure 3.2 *The different steps of the Langmuir–Blodgett and Langmuir–Schäfer depositions.*

Details about the LB film preparation of 100 mol % **V-79** and 40 mol % **PDI** in ODA are given in [I]. The preparation of **PHT** (60 mol % in ODA), **P–F**, and **F–P** (10 mol % in ODA) LB monolayers is described elsewhere.[168,169] The LS deposition of **P–F** is already described in [180,II], while the experimental details for the fabrication of LS films of **PHT** can be found in [III].

3.2.2 Vacuum thermal evaporation

The vacuum thermal evaporation is a common method for both organic and inorganic thin film depositions, which ensures smooth and homogeneous films with controllable layer thickness.

The source material is evaporated in high vacuum (typical pressure $\approx 10^{-6}$ mbar), and the vapor particles travel to a target object (substrate), where they condense back to the solid state.

In this work, a standard evaporation chamber was used. The organic compounds (**CuPc**, **C_{60}**, **PTCDI**, **Alq_3**) were evaporated from ceramic jars heated up to specific

temperatures (chosen according to the melting points of the compounds). The thickness of the evaporated films was monitored with a piezoelectric microcrystal balance, where a change in the resonance frequency of the crystal corresponds to the mass of the accumulated substrate. The crystals were calibrated by an optical profilometer. The reproducibility of the evaporated thicknesses could be checked through steady-state absorption spectrometry, as explained in Section 3.5.1.

The inorganic materials were evaporated in molybdenum boats or on tungsten wires to which current was applied. In the present work, Au has been mainly evaporated as metal electrode for solar cells,[II,IV,V] and in a few examples an Al electrode has been evaporated as top-cathode for comparison purposes.[IV,V]

3.2.3 Spin-coating

The spin-coating method is probably the easiest and fastest deposition technique for thin films for organic solar cells. An excess amount of solution of a selected compound is spread onto a substrate, which is then rotated at a given high speed. The centrifugal force causes the spreading of the solution on (and eventually also off) the substrate. During the spinning, the solvent evaporates and a uniform film of the solute is formed on the substrate. Films with desired thickness (typically from a few nanometers to micrometers) can be deposited by selecting the concentration of the solution, the solvent, and the spinning parameters.

In the present study, **PHT** has been deposited by spin-coating when used as HTL in photovoltaic devices.[I,V] **PHT** was spin-coated from a 2 g/l chloroform solution, due to its high solubility in this solvent which ensures homogenous films. The **H_2Pc–C_{60}ee** dyad has been earlier deposited by LB[98] or LS[181] methods. In [V], **H_2Pc–C_{60}ee** was spin-coated from a 4 g/l toluene solution, or first mixed with **PHT** in a chloroform solution (mass ratio 1:1, total concentration 3 g/l) and then spin-coated. In the solar cells, when **H_2Pc–C_{60}ee** was spin-coated as a separate film on top of a **PHT** spin-coated layer, this produced a noticeable damage to the **PHT** film which was partly washed and partly mixed with **H_2Pc–C_{60}ee**,[V] as discussed in Section 4.2.1. The phthalocyanine derivative **ZnPH4** was used for a few photocurrent measurements[I] as spin-coated films from a 3.3 g/l methanol solution.

3.3 Solar cell preparation

The photovoltaic devices investigated in this Thesis are based on multilayered organic thin film structures.[I,III–V] All the studied systems were fabricated onto glass

substrates coated with a transparent conducting ITO anode (sheet resistance about 8 Ω/sq). Different systems have been adopted as top-cathodes of the cells. In paper I, a three-electrode photoelectrochemical cell was studied, where the top-electrode consisted of an aqueous electrolyte solution containing an electron acceptor. In this system, the photogenerated electrons are transported from the topmost active layer of the film to the counter electrode by the acceptor in the electrolyte. The measurements were carried out in a three-electrode cell, having ITO as the working electrode (area = 0.28 cm^2), a Pt wire as the counter electrode, and Ag/AgCl (sat. KCl) as the reference electrode. The electron acceptor was 1,1'-dimethyl-4,4'-bipyridinium dichloride (methyl viologen, MV^{2+}), used in 5 mM concentration in aqueous electrolytic solution. The supporting electrolyte was 100 mM KCl.

In papers [II,IV,V] layered cells with solid top-electrodes were developed. A metallic cathode (Au or Al) was evaporated on the topmost organic layer through a mask to obtain a 1 mm^2 active area.

Prior to the organic film deposition, the substrates required thorough cleaning in ultrasonic bath with acetone, chloroform, isopropanol, sodium dodecyl sulfate

(SDS) solution, and finally with Milli-Q water. This was followed by the drying of the plates under N_2 flow at 150 ºC for 1 hour.

For the solar cells with metal top-cathode, part of ITO was removed from the plate by etching with *aqua regia* (concentrated HCl: concentrated HNO_3: H_2O in 4.6:0.4:5 ratio) after the cleaning of the substrates so as to prevent short circuit when contacting the cathode. Substrates were finally cleaned again in ultrasonic bath with the solvents mentioned above.

3.4 Photoelectrical measurements

In this Thesis different kinds of photoelectrical measurements have been carried out. The vectorial photoinduced ET in films was studied by the time-resolved Maxwell displacement charge (TRMDC) or photovoltage (PV) method.[I-III] The photocurrent (PC) measurements were performed to demonstrate that the studied film configurations could be used in photovoltaic devices. All of the photoelectrical measurements were carried out at room temperature, without protecting the active layers against air exposure.

3.4.1 Photovoltage

The TRMDC photovoltage method provides a powerful way to verify the vertical orientation of the donor and acceptor part in thin films.[18–20,166,168,170–174] The method is very sensitive, and it can be applied to ultrathin photoactive films without damaging them. Hence, it can be used to study the ET in organized LB/LS films, which can be ordered so that intermolecular ET can always be observed in a desired vertical direction. The scheme of the photovoltage measurement circuit is presented in Figure 3.3.

Samples were excited by a 10 ns laser pulse at 430 nm from the second harmonic of a titanium-sapphire laser (adjustable in the wavelength range 340–450 nm) pumped by the second harmonic of a Q-switched Nd:YAG laser (532 nm). Samples were excited also at 532 and 690 nm. A typical sample structure for the photovoltage (PV) measurements was ITO|11-12 ODA|active layers|20 ODA|InGa liquid-metal drop electrode (InGa). For simplicity in this Thesis the different sample structures will be referred to by presenting only their active layers configurations.

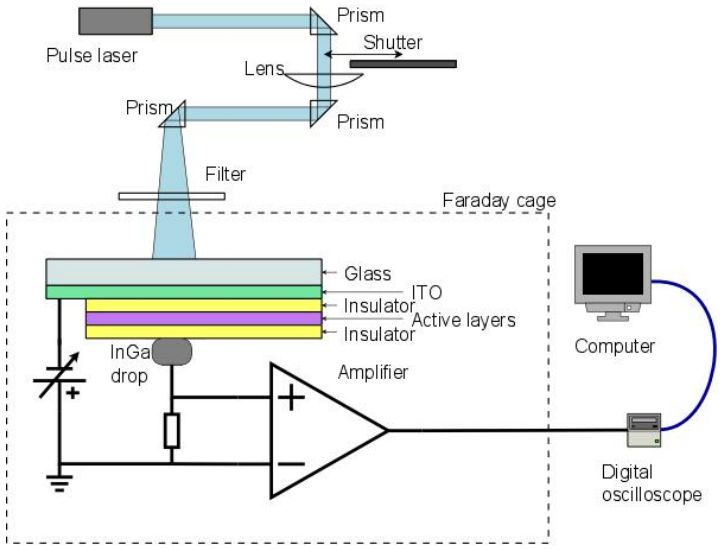

Figure 3.3 *Schematic view of the TRMDC photovoltage measurement circuit.*

Since the photoactive layers are insulated from the two electrodes (ITO and InGa), the measured PV signals are caused only by the electron movement inside the active layers, in a direction perpendicular to the plane of the films. The TRMDC measurements are carried out in a much shorter time domain than the instrumental time constant (~ 10 ms) of the measurement system,[172,175] thus the PV amplitude is

directly proportional both to the charge displacement and to the number of CS states.

The signal direction is connected with the direction of the displacement: negative signals are obtained when electrons move from ITO toward the InGa electrode and vice versa. Moreover, the signal decay describes the recombination of the CS states in the layers. The built-in electric field[175] due to the difference in the work functions of the electrodes (4.7 eV for ITO,[176] 4.2 eV for InGa[177]) can be cancelled by applying an external bias voltage of –0.5 V.

With the TRMDC method it is possible to detect the charge separation in a certain film structure, and to clarify the direction of the ET in films. However, the charges cannot be identified with this technique. In fact, it is not possible to distinguish between cationic or anionic species, and thus time-resolved spectroscopic methods are needed to characterize the ET reactions.

3.4.2 Solar cell characterization

Different types of measurements are required to fully characterize the performance of solar cells, namely the current–voltage (*I–V*) characteristics and the spectral photocurrent measurements. By recording the *I–V* curves, it is possible to determine the maximum power output, and thus the power conversion efficiency. From the spectral photocurrent measurements, the number of collected electrons per incident photon can be calculated. Hence these experiments are also called Incident Photon-to-Current Efficiency (IPCE) measurement.

I–V characteristics. Solar cells can be modeled as a current source in parallel with a diode.[178] Most of the photovoltaic performance parameters of a solar cell, as well as its electric behaviour, can be derived from the *I–V* characteristics, like the short-circuit current (I_{SC}), the open circuit voltage (U_{OC}), and the fill factor (*FF*). I_{SC} is the current which flows with zero load resistance (V=0, short circuit conditions), and it corresponds to the maximum current generated by the cell under illumination. U_{OC} is the voltage in conditions of open circuit, when no current flows through the cell. In other words, U_{OC} corresponds to the maximum possible voltage across the cell at zero output current. The *FF* is the ratio of the maximum power that can be drawn from the device (P_{MAX}) and the theoretical power (Eq. 1):

$$FF = \frac{P_{MAX}}{I_{SC}\ U_{OC}} = \frac{I_{MAX}\ V_{MAX}}{I_{SC}\ U_{OC}} \quad (1)$$

FF is directly related to the series and shunt resistance of the cell. Higher fill factors are achieved by increasing the shunt resistance and decreasing the series resistance. A larger *FF* is desirable, and corresponds to a more "square-like" shape of the *I–V* curve.

Figure 3.4 shows a schematic diagram of the *I–V* curves of an ideal photovoltaic cell in dark and under illumination. In darkness, no photocurrent flows through the cell, and the curve corresponds to that of a diode. With incident illumination, the device generates photocurrent and the *I–V* curve is shifted down in the fourth quadrant with respect to the curve in darkness (Figure 3.4). The power (*P*) produced by the cell can be calculated along the *I–V* sweep by the equation *P=IV*. The power is zero at the I_{SC} and U_{OC} points, and maximum (P_{MAX}) between the two points (shaded square in Figure 3.4).

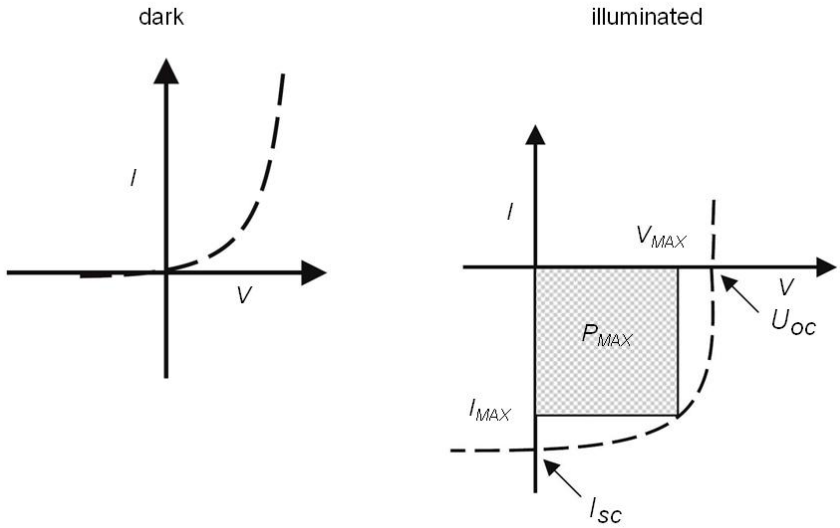

Figure 3.4 *Current–voltage (I–V) characteristics of an ideal solar cell in dark (left) and under illumination (right). In the I–V curve of the device under illumination, the intersections with the abscissa and the ordinate are the open-circuit voltage (U_{OC}) and the short circuit current (I_{SC}), respectively. The largest power output (P_{MAX}) is determined by the point where the product of voltage and current is maximized.*

The power conversion efficiency of the device (η) can be calculated from the defined parameters. η is the ratio of the maximum generated power to the incident optical power (P_0).[4] Hence, η can be expressed as follows (Eq. 2):

$$\eta = \frac{P_{MAX}}{P_0} = \frac{FF \cdot I_{SC} \cdot U_{OC}}{P_0} \quad (2)$$

In this work, the *I–V* characteristics were measured by using a standard source/monitor unit. In [I], the *I–V* measurements were carried out in darkness, and with an excitation light source coupled with a monochromator, used to select the excitation wavelengths. In [II,IV,V], the *I–V* curves were recorded in dark and under AM 1.5 sunlight illumination, produced with a filtered Xe-lamp in a solar simulator. All the measurements in this Thesis were carried out in air at room temperature, without encapsulation of the devices.

Spectral photocurrent measurements. Another way to characterize the solar cells, and to optimize their performance, is the measurement of their spectral response. These experiments are carried out by illuminating the devices by a monochromatic light source, and measuring the photocurrent as a function of the wavelength. The final IPCE spectrum is derived as the ratio between the number of generated electrons and the number of incident photons. In other words, the IPCE is a measure of the efficiency of the cell. The IPCE spectra are key measurements in the solar cell research. In fact, efficient photon harvesting requires the spectral response of the cells to match the spectral distribution of sunlight.

In [I,II,V], the cells were illuminated with monochromatic light provided by a Xe-lamp, and the wavelengths of the incident light were selected by a monochromator in the 400–800 nm range. The spectra were finally corrected by means of calibrated photodiodes.

3.5 Spectroscopic measurements

All the spectroscopic results presented here refer to measurements of absorption.
For spectroscopic studies, the films were deposited onto quartz substrates, cleaned by the standard procedure,[179] and plasma etched for 15 minutes in a low-pressure nitrogen atmosphere with a plasma cleaner. For time-resolved absorption experiments, the quartz plates had both ends polished to 45° angle.

3.5.1 Steady-state absorption

Steady-state absorption was used as a routine method to check the quality of the film depositions. In the LB/LS technology, a straightforward test of the reproducibility of the transfer of a chromophore containing monolayer onto a solid substrate (a quartz slide in this case) can be done by reporting the absorption of the

dye at the Soret-band as a function of the number of deposited layers. The absorption must increase linearly with increasing film thickness, in accordance with Beer's law.[I] In this work, such kind of test was routinely done in the film preparation step, to verify the reproducibility of the layer depositions especially for unknown compounds.

For evaporated films, an optical profilometer was used to determine the correlation between the absorption and the measured thickness, thus allowing controlling the reproducibility of film thicknesses.

Steady-state absorption spectroscopy enabled also identifying the excitation wavelengths for the photoelectrical and time-resolved spectroscopic measurements, based on the position of the characteristic Soret- and Q-bands for each molecule.

The steady-state absorption spectra for all the studied compounds in solutions and in films were recorded with a conventional UV-visible spectrophotometer with continuous light excitation in the 200–850 nm wavelength range.

3.5.2 Time-resolved absorption

The laser flash-photolysis setup (Figure 3.5) has been used here for the time-resolved absorption measurements in micro- to millisecond time scale. The method provides information on the transient states formed upon photoexcitation.

The sample is photoexcited by a strong laser pulse named pump. The changes in absorption are caused by the excitation of the molecules to higher energy levels provided by the pump pulse. The transient species generated by the light pulse present their distinct absorption characteristics, which result in absorption increases at specific wavelengths. The relaxation process, initiated by the pump pulse, is monitored by the probe, which is a pulsed or continuous light. In a time-resolved spectrum, the positive and negative absorption changes are monitored as a function of time at a given wavelength. The negative absorption arises from the reduced population in the ground state, which decreases the ground state absorption (bleaching) at the corresponding wavelengths.

The recombination of photoexcited molecules to their ground state can be followed by the signal decay.

The time scale of the flash-photolysis method is too slow to detect the formation of the transient intermediate states. As a result of this, only the final transient states of the film system can be observed. The flash-photolysis system was modified for total internal reflection mode in order to increase its sensitivity.[149]

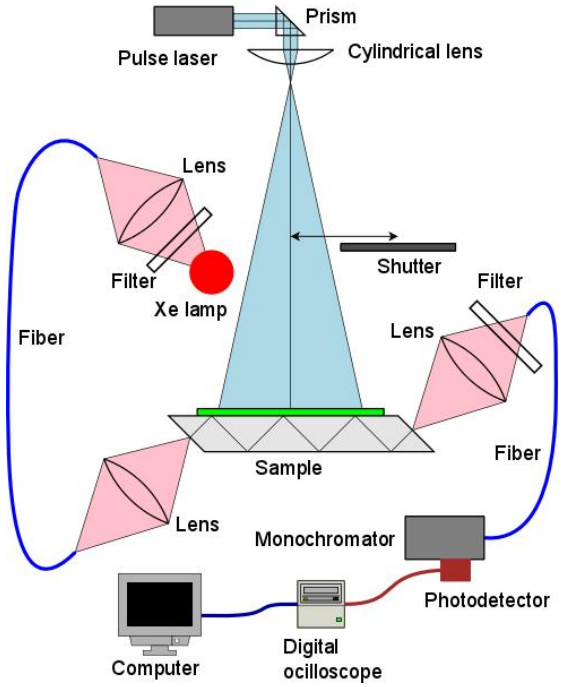

Figure 3.5 *Scheme of the laser flash-photolysis system.*

Continuous white light from a Xe-lamp was used as the probe. Samples were photoexcited at the wavelengths of 430 nm and 532 nm, using the same laser arrangement as in PV measurements.

Excitation energy density was ≈ 2 mJ/cm^2, at both the excitation wavelengths. The monitoring wavelength range was 460–1264 nm. The 600–1100 nm wavelength range was monitored by a photomultiplier tube in the visible part, and by using an additional monochromator and a detector in the near-IR region.

All the flash-photolysis samples were measured in nitrogen atmosphere, after being exposed to air in the film preparation step.

4 Results and discussion

In this chapter, the most significant results of publications I–V are summarized. First, the assembly of the studied film structures and their characterization is described. The intra- and interlayer ET in systems containing **P–F** and different *n*-type materials (**V-79**, **PDI**, **PTCDI**) is demonstrated by means of the TRMDC photovoltage technique.[I,II] The ET studies are also supported and clarified by laser flash-photolysis measurements.[II,III] It is subsequently shown that it is possible to observe photocurrent generation by building photoelectrochemical cells based on the studied film configurations. Finally, the fabrication of layered organic solar cells with solid top-electrode is described.[IV] Multilayered solar cells including HTL, D–A pair, and ETL are presented, and the role of the dyad in the devices is discussed.[V]

4.1 Assembling of the film structures

The knowledge of the energy levels (HOMO, LUMO) of the studied compounds is a crucial step in assembling the films of different molecules. In fact, it allows tuning the direction of electrons/holes in the structures. In Chart 4.1, a schematic view of the energy levels of the studied molecules is shown.

For **PHT**,[182] **ZnPH4**,[20] **CuPc**,[183] **C_{60}**,[184] **PTCDI**,[185] and **Alq_3**[153] the HOMO/LUMO energies are taken from the literature. For **P–F** (or **F–P**), **V-79**, **PDI**, and **H_2Pc–C_{60}ee** the energy levels are derived from differential pulse voltammetry (DPV) experiments, whose results are reported in Table 4.1.

Table 4.1 *Oxidation and reduction potentials (V_{OX}, V_{RED}), as derived from differential pulse voltammetry (DPV) experiments. The reported values are referred to the ferrocene standard.*

Compound	V_{OX}, eV	V_{RED}, eV
V-79	0.47	–1.21
PDI	1.23	–0.99
P–F	0.59	–1.06
H_2Pc–C_{60}ee	0.77	–0.76

From the DPV data, it is possible to derive the HOMO and LUMO energies for **P–F** (or **F–P**), **H_2Pc–C_{60}ee**, **V-79** and **PDI**, by taking into account the energy of the ferrocene reference (4.8 eV below the vacuum level[187]).

Chart 4.1 *Energy levels diagram of the studied compounds. The work functions of ITO, Au, Al, and the HOMO/LUMO energies of MV^{2+} are also reported.*

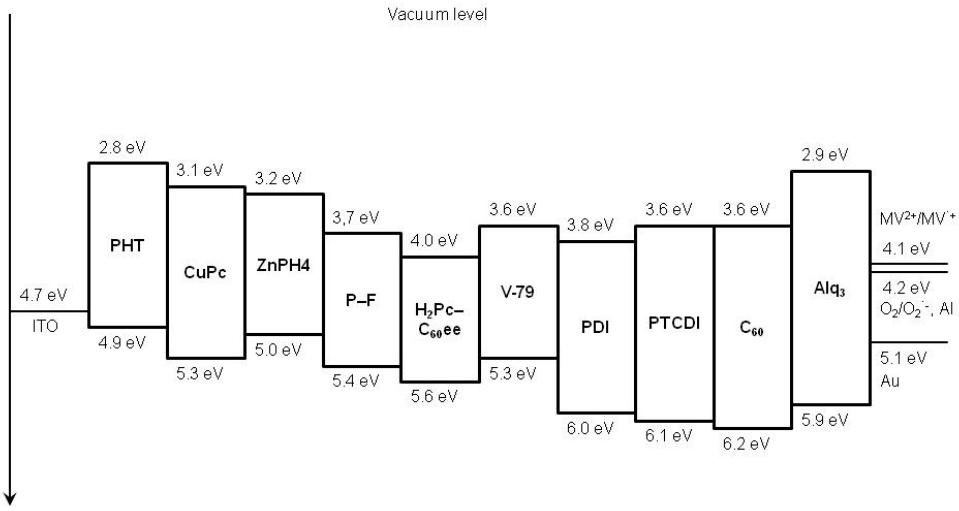

In addition, in Chart 4.1 the work functions of ITO,[176] Au,[187] Al[187] and the HOMO/LUMO energies of MV^{2+} (used in the photoelectrochemical cell) are given.

PHT and **ZnPH4** are known to give secondary electron donation to the porphyrin cation of **P–F**, as supported by the higher HOMO levels of the donors with respect to that of **P–F**. The strongest donor is **PHT**, which has the highest HOMO/LUMO levels, and thus it can donate electrons to other donors such as **ZnPH4**, or **CuPc**. Being the ITO work function higher than the HOMO levels of all the studied donors, this explains the possibility of hole transfer from the organics towards ITO.

C_{60}, **PTCDI**, and **Alq_3** are widely known ETL materials. Moreover, the energy levels of **V-79** and **PDI** reveal that both compounds could be used as electron acceptors for the fullerene anion of the dyad. **PDI** seems to be slightly more suitable than **V-79**, due to a better matching of its LUMO energy with that of the fullerene moiety of **P–F**. The reduction potential of MV^{2+} lies below the LUMO levels of the fullerene moiety of **P–F**, **V-79**, and **PDI**; this justifies the ET from the mentioned compounds to MV^{2+}. The LUMO level of **Alq_3** lies above that of the other acceptor, and thus this should not facilitate the ET from the acceptors through **Alq_3** towards the cathode. However, **Alq_3** is not used as a photoactive layer but as a buffer layer, and its presence should be considered as a modification of the cathode.[IV,V,II]

In most of the published solar cells, ITO is adopted as the high work function electrode (anode), and Al as the low work function electrode (cathode). In the solar cells presented in this Thesis, Au has been used as a cathode instead of Al (except

in a few examples for comparison) although its work function is higher than that of ITO. The coupling of Au with a thin **Alq_3** film resulted in a modification of the electrode work function, which made the electron collection possible, as will be described in Section 4.5.1.

The choice of Au in our cells was due to its high stability and reliability compared to Al, which undergoes fast oxidation in air accelerated by light exposure.

The layer arrangement for the photovoltage measurements is shown in Chart 4.2, where an example of active layers measured in [III] is also shown.

Chart 4.2 *Arrangement of the films in photovoltage experiments. The active layers presented as example (right side of the Chart) refer to a structure measured in [III].*

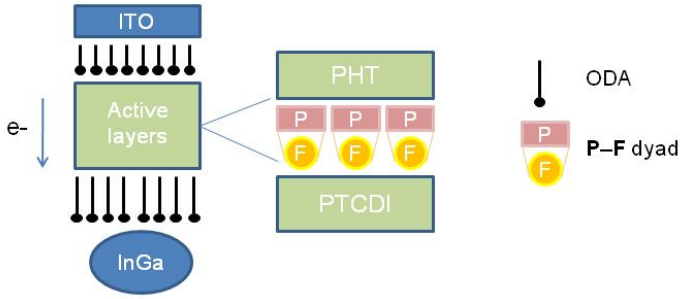

All the film configurations studied in this Thesis included single layers (electron-donor, dyad, or electron-acceptor), double layers (electron-donor and electron-acceptor, electron-donor and dyad), and trilayers (electron-donor, dyad, and electron-acceptor). In addition, for most of the sample configurations also the reversed structures were built as additional proof of the direction of the ET in the films.

The layer arrangement for the spectroscopic measurements (steady-state and time-resolved) is depicted in Chart 4.3. In the flash-photolysis measurements, a certain active layer configuration was repeated in the sample in order to increase the sample absorption and thus to achieve a reasonable signal-to-noise ratio. Four ODA layers were deposited between each of the deposited photoactive segments to insulate them one from the other (Chart 4.3b).

Chart 4.3 *Layer arrangement for steady-state (a) and time-resolved (b) spectroscopy measurements.*

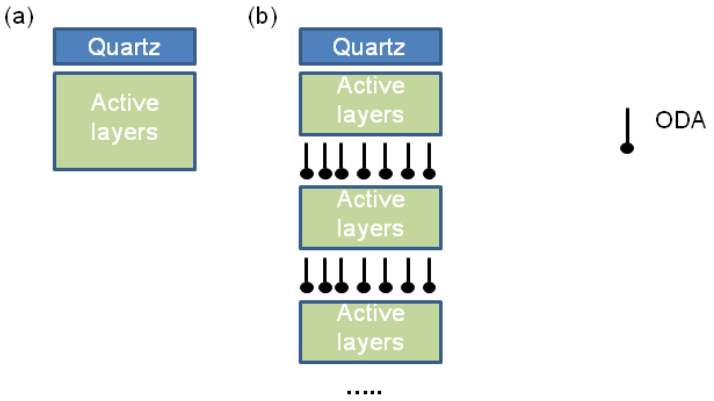

The device layout of the investigated solar cells is presented in Chart 4.4, where the most complex case of a multilayered cell containing both hole transporting layer, D–A pair, and electron transporting layer is presented. However, in the present work simpler configurations have been studied as well.[II,IV]

In the case of the photoelectrochemical cells,[I] the layout is similar to that depicted in Chart 4.4, but the metal top-electrode is replaced by a liquid cell containing MV^{2+} in an aqueous electrolyte. Moreover, no **Alq_3** layer is used on the top-most organic layer.

Chart 4.4 *Layout of the solar cells investigated in the Thesis.*

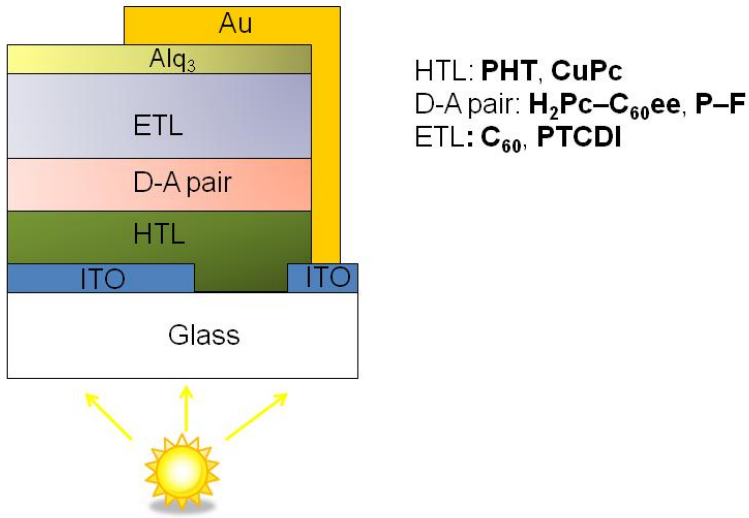

4.2 Film characterization

4.2.1 Steady-state absorption spectroscopy

The absorption spectra for the LB/LS monolayers of the studied compounds are presented in Figure 4.1. All the LB films in the figure were made by upward (water-to-air) deposition. The LS monolayers of **PHT** and **P–F** have significantly higher absorption than the corresponding LB films, which is expected since they contain 100 mol % of active molecules.

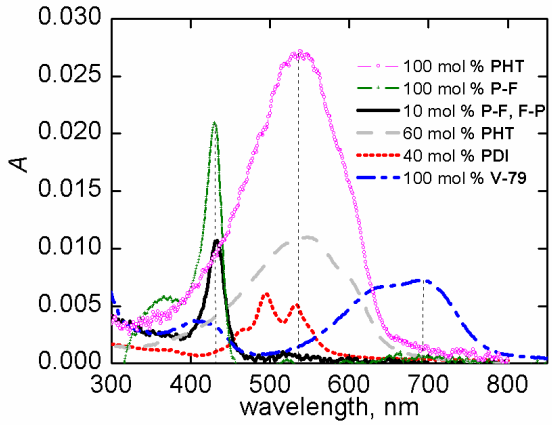

Figure 4.1 *Absorption spectra of the LB and LS monolayers of the studied compounds. In the legend, 100 mol % **PHT** and 100 mol % **P–F** refer to LS films, while all the others are LB films.*

P–F and **F–P** show a typical narrow absorption band with the maximum at 430 nm, corresponding to the porphyrin Soret-band (transition $S_0 \rightarrow S_2$). **PHT** has a broad absorption band centered at 540 nm. The **PDI** absorption maximum overlaps with the absorption of **PHT**, while **V-79** has a characteristic band at longer wavelengths with maximum at 690 nm.

In Figure 4.2, the absorption spectra of the spin-coated and evaporated films investigated in this Thesis are reported.

The spectrum of **CuPc** consists of strong transitions to the second excited state (Soret-band) around 345 nm, and weak transitions to the first excited state (Q-band) at 700 nm.[188,189] **C_{60}** has characteristic bands in the UV and the short-wavelength region of the visible spectrum, with maxima at roughly 350 and 450 nm. **PTCDI** shows a broad absorption with maxima between 500–600 nm, which overlaps with **PHT** absorption.

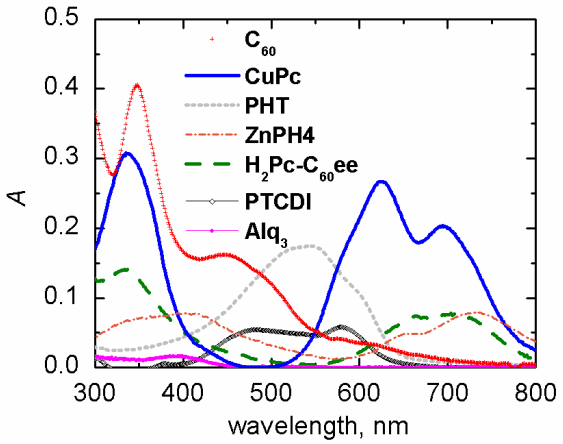

Figure 4.2 *Absorption spectra of the spin-coated (**PHT**, **ZnPH4**, **H_2Pc–C_{60}ee**) and evaporated (**CuPc**, **C_{60}**, **PTCDI**, and **Alq_3**) films studied in the Thesis.*

Alq_3 spectrum is characterized by a low-intensity absorption band centered at roughly 400 nm. The **H_2Pc–C_{60}ee** dyad has two main bands in the absorption spectrum: one centered around 350 nm, which arise from the **C_{60}** absorption and the Soret-band of the phthalocyanine, and another one with maximum at 710 nm, which corresponds to the phthalocyanine Q-band. The broader absorption of this dyad in the visible region compared to the **P–F** dyad ensures a better matching of **H_2Pc–C_{60}ee** with the spectrum of white light, making it potentially more interesting in photovoltaic applications.

Finally, **ZnPH4** has two main absorption bands: a Soret-band around 400 nm, and a Q-band (transition $S_0 \rightarrow S_1$) at 710 nm.

In the studied film structures, different molecular films have been combined in the same sample (multilayered structure) in order to obtain high absorption in a broad wavelength range. The multilayer usually consists of different components (donors, acceptors) having absorption maxima at different wavelengths. Thus, the spectrum of the resulting multilayered structure covers a wider region of the solar spectrum. It was seen that the overall absorption of the multilayer is a linear combination of the individual absorptions of its molecular layers, thus indicating a weak spectroscopic interaction between the molecules of different layers in their ground state.

When **H_2Pc–C_{60}ee** was spin-coated on top of a **PHT** spin-coated layer,[V] the absorption of the bilayer was slightly lower than that calculated by the superimposition of the absorption spectra of the individual components, as evaluated from the experimental absorption spectrum.[V] Most deviation is observed

around 500–600 nm, and it is due to the reduction in the absorption of the **PHT** layer which is partly washed away and partly mixed with **H_2Pc–C_{60}ee**.

4.2.2 Atomic Force Microscopy (AFM) and profilometry

An Atomic Force Microscopy (AFM) characterization of some of the investigated films was required in order to monitor the film quality and to examine the film morphology at nanometric scale. AFM studies were carried out for **V-79** and **PDI** monolayers, deposited on silicon substrates by the LB technique.[I] **V-79** films appeared smooth and uniform, and showed quite an organized fine structure.

PDI molecules highly aggregate and phase-separate when mixed in an ODA matrix. Globular **PDI** clusters about 3-4 nm in height were found. The overall film quality of **PDI** was poorer compared to **V-79**. The AFM images of **V-79** and **PDI** can be found in the Supporting Information of [I].

LS films of **P–F** and evaporated **PTCDI** layers were also studied by AFM.[II] **P–F** and **PTCDI** were deposited on silicon and mica substrates, respectively. The AFM topographs (in the Supporting Information of [II]) show that both **P–F** and **PTCDI** form relatively smooth and uniform films after deposition. However, the roughness analysis indicates that the **P–F** film is somewhat rougher compared to **PTCDI** film. If the AFM image of **P–F** as 10 mol % LB film[168] is considered for comparison, it can be noticed that, even though the dyads form flat films, they are not homogenously distributed over the monolayer area. In case of LS films of **P–F**, the lack of ODA ensures homogenous distribution of dyad molecules, as well as an enhanced surface coverage of **P–F** in the films, which will result in more efficient photoelectrical signals, as discussed later.

The comparison between the AFM micrographs of the two perylene derivatives, **PDI** and **PTCDI**, suggests the use of **PTCDI** evaporated films for ET/solar cells applications due to the smaller roughness and higher homogeneity.

The thickness of the films was estimated by profilometry measurements deposited onto quartz slides. The average thicknesses for **V-79** and **PDI** LB monolayers were 1 and 2.5 nm, respectively. For the other LB films presented in the Thesis, the monolayer thicknesses were already known from previous studies (thickness = 2 nm for 10 mol % **P–F** monolayer in ODA,[20] thickness = 3 nm for 60 mol % **PHT** LB monolayer in ODA[18]). The thickness of a LS monolayer of **P–F** (100 mol %) was estimated to be 2.5 nm,[II] while that of **PHT** monolayer (100 mol % LS film) was 3 nm.[III] The thickness of the thermally evaporated films (**CuPc**, **C_{60}**, **PTCDI**, **Alq_3**) was monitored by quartz crystals during the evaporation, and

could be easily adjusted to the desired value. In the Thesis, **PTCDI** thickness varied from 5 to 40 nm, depending on the measurement. In solar cell applications, typically the total thickness of the cell active layers was in the range 45–90 nm, according to the sample structure.

4.3 Photoinduced electron transfer

The intra- and intermolecular ET in multilayered film structures was thoroughly studied by the TRMDC photovoltage and laser flash-photolysis techniques. The understanding of the photoinduced processes taking place in organic thin films was the first crucial step toward the development of photovoltaic cells.

4.3.1 V-79 and PDI as novel electron-acceptors in LB films

The capability of **V-79** and **PDI** to act as electron acceptors, with respect to **PHT** and to the photoinduced fullerene anion of **P–F** dyad, was tested in LB films by the photovoltage method.[I]

Double layers were constructed by combining molecularly controlled LB films of **PHT**, **P–F**, **F–P**, **V-79** and/or **PDI**.

Let us consider first the samples containing **V-79**. The PV responses of **PHT**|**V-79** and **V-79**|**PHT** were measured at the excitation wavelengths (λ_{exc}) of 532 nm (where mainly **PHT** is excited) and 690 nm (where **V-79** has its absorption maximum). A response with negative polarity was observed for **PHT**|**V-79**, while a nearly mirror image of positive polarity signal was observed for the **V-79**|**PHT** structure (Figure 4.3). This result indicates ET from **PHT** to **V-79** independently of which chromophore is photoexcited.

Similar experiments were carried out with **P–F** and **V-79**. According to the orientation of **V-79** and **P–F** (or **F–P**) with respect to ITO (*i.e.*, whether **P–F** or **V-79** are deposited from the ITO side), two different polarities of the signals were obtained. When **V-79** was on top of fullerene (**P–F**|**V-79**) the signal was negative. On the contrary, when it was deposited under the fullerene layer (**V-79**|**F–P**) the signal was positive. From these results one can conclude that **V-79** is able to accept electrons from **P–F** dyad, when either **P–F** or **V-79** is excited.

The amplitudes of the PV signals are shown in Table 4.2 as sensitivity, voltage divided by the excitation energy density (V cm^2/mJ).

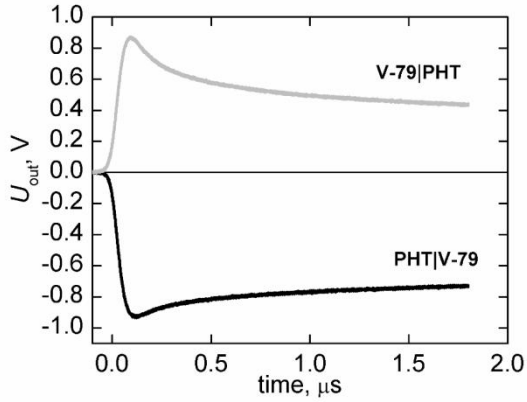

Figure 4.3 *Photovoltage responses of the* ***PHT|V-79*** *and* ***V-79|PHT*** *structures at the excitation wavelength (λ_{exc}) of 690 nm.*

Table 4.2 *Photovoltage response amplitudes (reported as sensitivities) for the described sample structures, at specific excitation wavelengths.*

Active layers	PV amp. at 430 nm, V cm^2/mJ	PV amp. at 532 nm, V cm^2/mJ	PV amp. at 690 nm, V cm^2/mJ
V-79	–0.01	–0.03	–0.07
PDI	–0.02	–1.22	--
PHT	--	–2.15	--
P–F	–0.17	–0.04	--
V-79|PHT	--	8.49	--
PDI|PHT	--	110	--
V-79|F–P	0.28	--	--
PDI|F–P	11.34	--	--
PHT|V79	--	–17.50	–10
PHT|PDI	--	–133	--
P–F|V-79	–1.48	--	–0.25
P–F|PDI	–44.60	–21	--

For the sake of completeness, the photovoltage responses for single layers (**PHT**, **V-79**, or **PDI**) were also measured. At the zero bias voltage, all unoriented single layers produced negative signals,[175] but their amplitudes were very low (see Table 4.2).

The comparison of the amplitudes of single layers and bilayers at the excitation wavelength of 532 nm revealed that the PV amplitude of the bilayer structure **V-79|PHT** is about 4 times higher with opposite sign than the sum of the amplitudes of individual **PHT** and **V-79** layers. Similarly, when exciting the structure **V-79|F–P** at 430 nm, roughly 2 times higher amplitude with opposite sign was obtained, compared to the sum of **F–P** and **V-79** layers. The PV amplitude is proportional to

the charge separation distance and to the number of CS states. However, the number of CS states can be assumed unchanged because the total absorption is the same. Hence, the increase in the signal amplitudes of the bilayers, compared to those of the single layers, can be attributed to the increased charge separation distance.[172]
In the bilayer **P–F** |**V-79**, a two-step ET process takes place. First, an intramolecular electron transfer occurs in the dyad from **P** to **F**. This is followed by a secondary ET from the fullerene radical anion in **P–F** to **V-79**. Such a multistep vectorial ET is supported by several other studies, where the secondary ET takes place mainly from a donor (*e.g.*, **PHT**) to the porphyrin cation of **P–F**.[18,20,174]
Similar structures as those with the **V-79** acceptor were made with the **PDI** acceptor, by using the same donors (**PHT**, **P–F**). Similarly, the PV results (Table 4.2) support a vectorial ET process from **PHT** or **P–F** to **PDI**.

The comparison between the increases of the amplitudes for **PDI** samples (by taking the absorption changes into account) and those for **V-79** samples shows that **PDI** is a stronger electron acceptor than **V-79**, and that the most efficient ET takes place between **P–F** and **PDI**.

Another difference between the **V-79** and **PDI** samples relates to the shape of the photovoltage responses, which in turn is associated with the lifetime of the CS state. The PV signals of all the presented structures were quite long-lived, in timescale from μs to ms. However, the **PDI** structures had longer lifetimes than the **V-79** ones.[I]

The addition of a **V-79** or **PDI** layer on top of **P–F** increased the lifetime of the CS state.[I] The longer lifetime of bilayer systems implies that the recombination of the separated charges in the trilayered system (*e.g.*, **P–F|V-79**) is retarded compared to the dyad alone. This is an additional proof that the primary charge separation (taking place in **P–F** or **F–P**) is extended in time by the secondary ET from the fullerene anion to the acceptor.

The photoinduced interactions between **V-79** and **PDI** were also studied, by measuring bilayered structures containing single layers of **V-79** and **PDI** (**V-79**|**PDI**, **PDI**|**V-79**). The experiments, explained in more detail in [I], revealed that **PDI** is able to accept electrons from **V-79**, thus behaving as electron-acceptor toward **V-79**.

Finally, the influence of the number of acceptor layers on the PV responses was studied in order to understand if the charge separation in a multilayered sample (which contains several acceptor layers) is limited not only by the interface between donor and acceptor but also by the acceptor layers. The measured samples were

constituted by a donor monolayer (**PHT** or **P–F**) and by 2, 6, and 12 **V-79** or **PDI** layers.

A detailed description of the experimental settings, and of the PV results of the multilayered structures can be found in [I]. These experiments show that, in the case of samples containing **P–F** and **PDI** excited at 430 nm, the PV amplitudes always increased when increasing the number of **PDI** layers. This can be explained by considering the ET through **PDI** layers, which originates from the diffusion of charges inside **PDI** layers. Similar results were found for structures containing **P–F** and **V-79**, which revealed that the ET through the layers seems more affected by the number of layers in **V-79** than in **PDI** samples. This originates from the higher electron conductivity of **V-79** films compared to **PDI** ones, which in turn derives from the fact that **V-79** films are 100 mol %, while **PDI** layers contain 60 mol % ODA matrix. ODA is an insulator, which decreases the conductivity of the films. Moreover, ODA is an inert matrix, and thus it reduces the coverage of active molecules in the films. Hence, the higher the ODA ratios are, the lower the probability of an interaction between two active sites is.

In samples containing **PHT** and **PDI**, the increase in the PV amplitudes with the **PDI** thickness was not very significant when the rise in the absorbance at the excitation wavelength is taken into account. This can be understood considering that PV signals are affected only by photons absorbed in the **PHT** layer.

Differently, for **PHT** and **V-79** samples, the significant increase in the PV amplitudes with the number of layers suggests that the ET proceeds through the **V-79** layers.

4.3.2 P–F dyad and PTCDI: ET in 100 mol % films

In the previous section, a vectorial ET from molecular films of dyads to selected electron acceptor layers was demonstrated.[I] In [I], the LB technique has been adopted to prepare films and, in most of the cases, an ODA matrix had to be mixed with the active molecules in order to obtain good quality LB films. Based on the idea that ODA is an insulator, and its introduction could decrease the conductivity of the films, the next goal of our research has been to build molecular film structures constituted by active molecules alone, and to study the intra- and intermolecular ET in such film systems. To this aim, two compounds were selected: the **P–F** dyad, deposited as 100 mol % LS film, and **PTCDI**, which was thermally evaporated.

PTCDI is studied here as electron-acceptor for **P–F** by using photoelectrical and spectroscopic methods.[II] The starting point for this study was the secondary ET observed to take place from **P–F** in CS state ($\mathbf{P^+–F^-}$) to a different perylene derivative (**PDI**), as shown in Section 4.3.1. However, in such a system the **PDI** films were not smooth, and the surface coverage by **PDI** molecules was poor.[I]

The photoinduced responses in film structures obtained by replacing **P–F** deposited by 10 mol % LB film with the 100 mol % LS film, and **PDI** (as 40 mol % LB film in ODA) with evaporated **PTCDI**, were compared with those of similar systems with ODA matrix investigated in [I].

TRMDC photovoltage. To prove the ET from **P–F** to **PTCDI**, several sample configurations have been tested by PV method at the excitation wavelengths of 430 and 532 nm. A bilayer structure containing **P–F** and **PTCDI** was compared with the corresponding reference samples of **P–F** monolayer (thickness = 2.5 nm), and **PTCDI** single layer (thickness = 16 nm).

The two possible orientations of **P** and **F** moieties of dyad with respect to the electrodes were investigated (molecules **P–F** and **F–P**). The intramolecular ET in the dyad is already well-known in case of 10 mol % LB films: two opposite polarities of PV signals are obtained for **P–F** and **F–P**, as demonstrated also in this study.[II] The other reference sample, **PTCDI**, showed a negative PV response, typical of non-oriented molecular layers.

The PV responses for the bilayers **P–F**|**PTCDI** and **PTCDI**|**F–P** at the excitation wavelength of 430 nm are reported in Figure 4.4, while the signals for the reference samples can be found in the Supplementary Information of [II]. The signal amplitudes for all the measured structures are reported in Table 4.3 as signal sensitivities (V cm^2/mJ).

The ET from **P–F** to **PTCDI** is demonstrated by the opposite polarity of the PV responses in Figure 4.4 for the **P–F**|**PTCDI** (negative polarity signal) and **PTCDI**|**F–P** (positive polarity signal) configurations. The comparison between the amplitudes of the bilayer samples and those of the reference samples shows that electrons can move through the whole bilayer system. At 430 nm, the amplitude of **P–F** |**PTCDI** is 25 times higher than the sum of the amplitudes of **P–F** and **PTCDI**. Since the absorption of the bilayer sample is the same as the sum of absorptions of **P–F** and **PTCDI**, such increase in the bilayer is attributed to the increased CS distance.

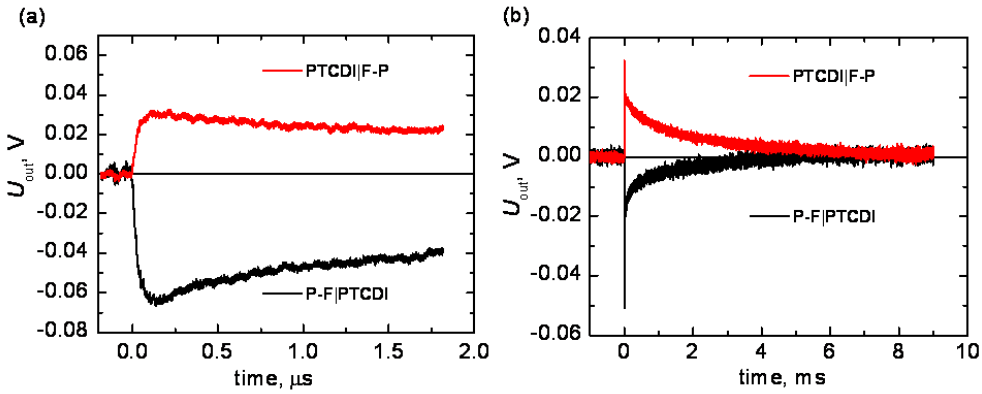

Figure 4.4 *Photovoltage responses in a short timescale (a) and in a long timescale (b) for the bilayers* ***P–F\PTCDI*** *and* ***PTCDI|F–P****. The excitation wavelength is 430 nm, and the excitation energy density 0.04 µJ/cm*^{2}.

Table 4.3 *Photovoltage response amplitudes (as sensitivities) for the described sample structures, at specific* λ_{exc}.

Active layers	λ_{exc}, nm	PV amp., V cm^2/mJ
P–F	430	–1.2
	532	--
F–P	430	0.4
	532	--
PTCDI	430	–63
	532	–97
P–F|PTCDI	430	1610
	532	–814
PTCDI|F–P	430	905
	532	1185

The long-lived behaviour of the bilayer systems, which decay to zero in about 9 ms,[II] can be also explained with the increased charge separation distance in **P**$^+$**–F|PTCDI**$^-$ film structure, followed by a lateral charge migration in the **P**$^+$ and **PTCDI**$^-$ layers.[19,20]

A comparison between the PV responses of Table 4.3 and those of similar systems with ODA matrix[I] reveals a significant increase in the sensitivities (several tens of times according to the sample structure) for the films with 100 mol % of active molecules. Possible explanations are the enhanced coverage of active molecules in the films and the different photoinduced interaction between the two compounds (**P–F** and **PTCDI** compared to **P–F** and **PDI**).

The ET from **P–F** to **PTCDI** takes place independently of which molecular layer is photoexcited, but the PV amplitude of **P–F**|**PTCDI** at the 532 nm excitation is roughly 2 times lower than that at 430 nm (see Table 4.3). For **PTCDI**|**F–P** sample the amplitudes are the same at both the excitation wavelengths, but the absorptions of the bilayer structures at 532 nm are approximately 2 times higher than those at 430 nm. This reveals a roughly two times less efficient ET from **P–F** to **PTCDI**, when only **PTCDI** is photoexcited at 532 nm, which in turn suggests that the excitation energy is utilized for other process than interlayer ET. For example, an energy transfer process could take place from **PTCDI** to the dyad, followed by ET from the dyad in CS state to **PTCDI**, as proposed in [181]. Another possible mechanism triggered by the 532 nm excitation is the ET from porphyrin moiety of **P–F** to the excited **PTCDI**.

At 430 nm, the mechanism of the ET is quite clear, since many studies report the fast and efficient ET from **P** to **F**, yielding a fullerene anion when the porphyrin moiety of **P–F** is excited.[147,168] In this sample series, both **P–F** and **PTCDI** absorb light at the 430 nm excitation. However, since the ET in **P–F** is very fast, the dominant process is a multistep ET: a primary intramolecular ET in **P–F** (forming $\mathbf{P^{+}–F^{-}}$), followed by a secondary ET from the fullerene anion to **PTCDI**.

Time-resolved absorption. The conclusions on the ET between **P–F** and **PTCDI** were confirmed and clarified by the laser flash-photolysis measurements. The **P–F**|**PTCDI** sample and the **P–F** and **PTCDI** references were studied. As mentioned in Section 4.1.3, each active layer configuration was repeated 6 times in the measured structures, so as to increase the sample absorption and thus to achieve a reasonable signal-to-noise ratio. All the samples were measured in similar conditions at the excitation wavelengths of 430 and 532 nm, with energy density of roughly 2 mJ/cm^2.

The time-resolved absorption spectra of **P–F** and **P–F**|**PTCDI** at 5 µs after the 430 nm excitation, recorded in the wavelength range of 600–1100 nm, are shown in Figure 4.5. The spectrum of **PTCDI** single layer is not presented since the flash-photolysis response is weak,[II] and thus the shape of **PTCDI** transient spectrum does not influence that of the **P–F**|**PTCDI** bilayer.

The **P–F** spectrum is coherent with that presented in a previous work, where the transient band around 750 nm is assigned to the porphyrin radical cation,[5,190,191] and the bleaching at 600 and 660 nm is detected for the porphyrin Q-band. Moreover, in the near-IR-region, the broad transient absorption in 850–1050 nm range is found, which is attributed to the fullerene anion radical.[191] The observed transient states

support the CS between porphyrin and fullerene ($\mathbf{P^+–F^-}$), which is consistent with the PV results and with previous studies.

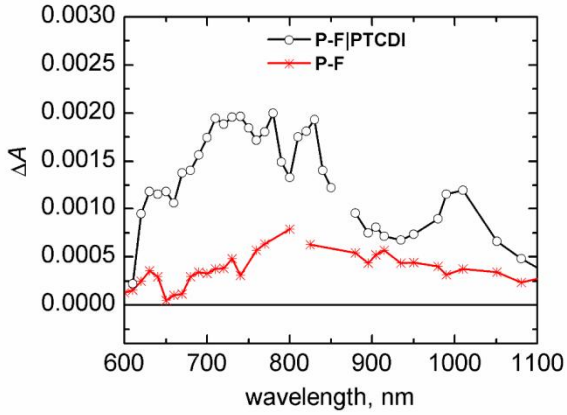

Figure 4.5 *Time-resolved absorption spectra of* ***P–F*** *and* ***P–F|PTCDI*** *film structures at 5 µs after the excitation. The* λ_{exc} *was 430 nm, and the excitation energy density was roughly 2* $\mu J/cm^2$.

In the time-resolved spectrum of **P–F|PTCDI** (Figure 4.5), three main transient bands are observed around 700, 820, and 1000 nm, corresponding to the **PTCDI** radical anion absorptions.[192] In the bilayer spectrum, the bleaching of the porphyrin Q-band is detected at 660 nm, while the porphyrin cation absorption at 750 nm is covered by the **PTCDI** anion absorption. The observed transient bands of porphyrin cation and **PTCDI** anion demonstrate the interlayer ET from **P–F** to **PTCDI**, producing the final transient state of $\mathbf{P^+–F|PTCDI^-}$.

The time-resolved absorption spectrum of **P–F|PTCDI** was recorded also at 532 nm excitation, where only **PTCDI** absorbs light. The comparison between the spectra of **P–F|PTCDI** at both the excitation wavelengths (430 and 532 nm) is shown in Figure 4.6. The shapes of the spectra correlate well one with the other, with small differences at 800 nm and 1000 nm. Thus, it can be concluded that the **PTCDI** anion and porphyrin cation are formed regardless of which chromophore is photoexcited (as in the PV measurements). The difference in the shape of the spectra recorded with different excitation wavelengths could be explained by considering the possible recombination of **PTCDI** anion to the triplet state at 532 nm, as suggested in literature for a different perylene derivative.[193–195] The possibility of triplet state recombination is also supported by the previous

considerations on the ET between **P–F** and **PTCDI**, whose total efficiency was lower when only **PTCDI** was photoexcited.

Another difference in the transient absorption spectra at the two excitation wavelengths is that the spectrum recorded at 532 nm excitation is mainly below that of 430 nm excitation (despite the higher absorption and number of photons at 532 nm). This confirms that the interlayer ET from **P–F** to **PTCDI** is more efficient upon the 430 nm excitation, as concluded in the PV results. This indicates that the major interlayer ET mechanism is the ET from the fullerene anion of the dyad to **PTCDI** at the 430 nm excitation, whereas at the 532 nm excitation wavelength the ET pathway is less clear. An energy transfer from excited **PTCDI** to **P–F** can take place, followed by the known primary and secondary ET reactions, and/or the ET from the porphyrin moiety of **P–F** to excited **PTCDI**. In both cases, the final transient state is **P**$^{+}$**–F|PTCDI**$^{-}$.

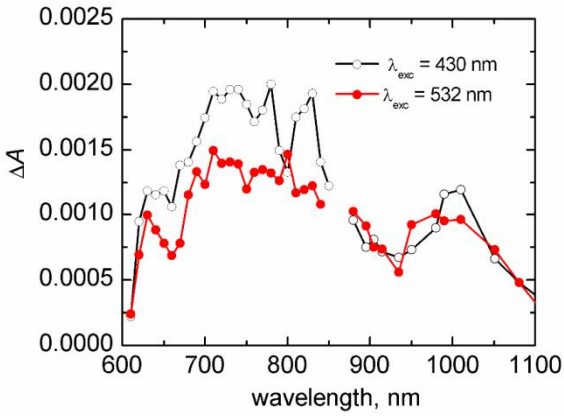

Figure 4.6 *Time-resolved absorption spectra of* ***P–F|PTCDI*** *film at different excitation wavelengths (430 nm and 532 nm). The spectra were recorded at delay time of 5 µs after the excitation.*

4.3.3 Multistep ET in PHT|P–F|PTCDI systems

If the complexity of the **P–F|PTCDI** system studied in Section 4.3.2 is increased with the introduction of a secondary electron-donor to **P–F**, a more efficient final charge separation can be achieved, with a consequent prolonged lifetime of the CS state. This could be a pivotal advantage when designing organic photovoltaic devices.

To this aim, a three-layer structure consisting of a HTL, D–A pair, and ETL was studied, where **PHT** was adopted as HTL material. The expected multistep ET

taking place through 100 mol % films of **PHT**, **P–F**, and **PTCDI**, deposited by the LS technique **(PHT**, **P–F**) and thermal evaporation (**PTCDI**), was carefully investigated by photoelectrical and spectroscopic methods. Moreover, the **PHT**|**PTCDI** structure, which forms an interesting heterojunction for organic solar cell applications, was studied for the first time.

TRMDC photovoltage. The complete set of the investigated film structures is shown in Table 4.4, where the PV response amplitudes of the multilayered structures and of the reference samples containing single layers of **PHT**, **P–F**, or **PTCDI**, are reported. For all the structures, the excitation wavelengths were 430 and 532 nm.

Table 4.4 *Photovoltage response amplitudes (as sensitivities) for the described sample structures, at specific excitation wavelengths (λ_{exc}).*

Active layers	λ_{exc}, nm	PV amp., Vcm^2/mJ
PHT	430	–13
	532	–29
P–F	430	–1.2
	532	--
PTCDI	430	–63
	532	–97
PHT|**PTCDI**	430	–2766
	532	–3354
PHT|**P–F**|**PTCDI**	430	–3001
	532	–2891

In Figure 4.7, the PV response amplitudes are shown as a function of time for the studied bilayer and trilayer structures.

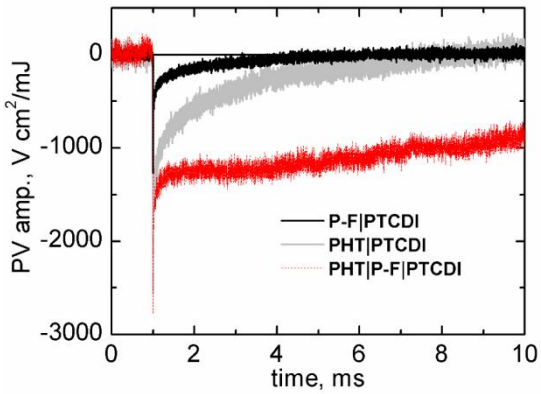

Figure 4.7 *Photovoltage responses in ms timescale for the* ***P–F|PTCDI*** *and* ***PHT|PTCDI*** *bilayers, and for the* ***PHT|P–F|PTCDI*** *trilayer. The excitation wavelength was 430 nm.*

Due to the instrumental set-up, the observed negative polarity of the PV signals indicates that electrons transfer from ITO towards InGa. Nevertheless, this does not prove that the ET proceeds through the whole layer system. To this aim, also the PV amplitudes should be taken into account, and compared with those of the single layers. As can be seen in Table 4.4, the PV sensitivity of **PHT|P–F|PTCDI** structure is 3000 V cm^2/mJ at 430 nm excitation, which is roughly 40 times higher than the sum of the amplitudes of **PHT**, **P–F**, and **PTCDI**, alone. This proves that the increase in the PV amplitude arises from the increased charge separation distance, which indicates that electrons move through the multilayers. Furthermore, the bigger amplitude of the TRMDC signals obtained for the trilayer structure with respect to the **PHT|PTCDI** configuration arises from the reduction in the recombination rate due to the fast ET from **F** to **PTCDI**, and to the hole transfer from **P** to **PHT**. Such effect is shown in the signal height rather than in the shape of the decays, since the geminate recombination takes place in a much shorter timescale than the experimental limit of the TRMDC method.

In Figure 4.7, there is a clear difference between the responses of the **P–F |PTCDI** and **PHT|P–F|PTCDI** structures in terms of the signals lifetime. The addition of **PHT** prolongs the lifetime of the CS state of the system. This is a strong proof of the efficient electron transfer through the layers. The increased CS distance retards the undesired charge recombination. This makes such film structures suitable for applications like solar cells, for which a long lifetime of the

nonrecombined charges is an important prerequisite to allow the photogenerated charges migrating to the respective electrodes.

The results discussed in this section referred to the PV signals achieved at the 430 nm excitation. Similar conclusions on the multistep through **PHT**, **P–F**, and **PTCDI** films can be drown from the results obtained by exciting the **PHT** and **PTCDI** absorption bands at 532 nm.[III]

Time-resolved absorption. The PV experiments showed that the ET proceeds through the whole **PHT**|**P–F**|**PTCDI** structure, giving rise to the final charge separation between **PHT** and **PTCDI**. By the time-resolved absorption experiments it is possible to demonstrate the ET processes between the individual components of the structures by identification of the final transient states.

The time-resolved absorption spectra of the studied film structures are presented in Figure 4.8. The spectra were recorded at 5 µs after the excitation with energy density of roughly 2 mJ/cm^2.

From the literature it is known that the **PHT** cation[149] absorbs at 650 nm and between 840–900 nm,[196] while the porphyrin cation has absorptions below 500 nm and around 750 nm.[5,190,191] The fullerene anion absorbs in the 850–1050 nm wavelength region[191] and the **PTCDI** anion absorbs around 700, 820, and 1000 nm.[192] In the transient absorption spectrum of the **PHT**|**P–F**|**PTCDI** structure (see Figure 4.8) the transient states, corresponding to the **PHT** cation at 840 nm and to the **PTCDI** anion absorptions at 820 and 1000 nm, can be identified. Both species absorb also in the visible region around 650–700 nm.

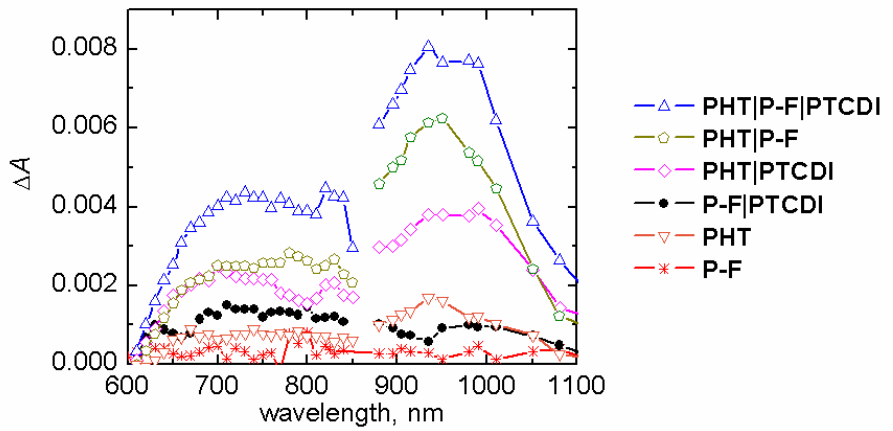

Figure 4.8 *Time-resolved transient absorption spectra of the most significant film structures at the excitation wavelength of 532 nm. The spectra were recorded at delay time of 5 µs after the excitation.*

.

Additional proof of the existence of ionic states is obtained by comparing the spectrum of a trilayer structure with the simpler structures in Figure 4.8. The addition of **PTCDI** to the **PHT**|**P–F** structure results in an increase in the signal amplitude and in a broadening of the absorption band at the IR region. This is due to the contribution of the **PTCDI** anion absorption, which can be detected in the trilayered structure at 700 nm, 820 nm, and around 1000 nm. The shapes of the transient absorption bands of the **PHT**|**P–F**|**PTCDI** and **PHT**|**PTCDI** spectra are practically identical, suggesting the same final states, *i.e.*, the **PHT** cation and **PTCDI** anion, in both structures. However, the trilayer structure shows higher absorption change than the bilayer structure. This indicates an efficient increase in the number of CS states when **P–F** is added to the film, as was demonstrated by the PV method as well.

The comparison between the transient absorption spectra of the **PHT**|**P–F**|**PTCDI** and **P–F**|**PTCDI** structures reveals that the addition of **PHT** increases the signal amplitudes significantly. Such an enhancement is attributed to the more efficient CS, which prolongs the lifetime of the structure.

The reference samples (**PHT** and **P–F** films) showed signals of very low-intensity, as shown in Figure 4.8. In the **PHT** spectrum, the **PHT** triplet state can be identified in the near-IR region at 940 nm. The **P–F** spectrum was described in Section 4.3.2. The **PTCDI** reference sample produced a very weak signal, as was shown earlier.

The normalized flash-photolysis decays of the most interesting film structures monitored at 1010 nm are presented in Figure 4.9. For all the structures, a fast recombination of the signal is followed by a longer-lived tail.

The transient states of the **PHT**|**PTCDI** structure recombine faster than in the other structures. The half-lifetime of the decay is 110 μs, and a complete decay lasts about 1 ms. The longer lifetime of the trilayered structure (half-lifetime = 140 μs) is due to the increased distance of CS resulting from the interlayer ET between **PHT**, **P–F**, and **PTCDI** layers. However, in this series the **PHT**|**P–F** structure has the longest lifetime, *i.e.*, 170 μs, even though it is very similar to that of the **PHT**|**P–F**|**PTCDI** structure. In the trilayered structure, the imperfection of the dyad layer, *e.g.*, possible holes in the film, which induce a direct contact between the **PHT** and **PTCDI** layers, might cause a faster decay.

The introduction of **PHT** in all the studied configurations was crucial for achieving longer lived CS.

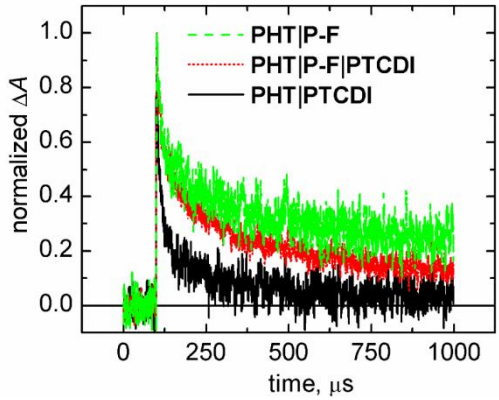

Figure 4.9 *Transient absorption decays of the most important film structures at the monitoring wavelength of 1010 nm. The excitation energy density was approximately 2 mJ/cm^2, and the excitation wavelength 532 nm.*

Lifetime of electrical and optical signals. Photovoltage and flash-photolysis techniques were used to monitor the final transient CS state of the structures. Hence, one should expect the lifetimes of the electrical and optical signals to be the same. However, the lifetimes of the electrical signals are in all cases longer than those of the optical ones.[III] A similar phenomenon was observed in previously published results as well.[21]

A possible explanation for the discrepancy in lifetimes could be based on the difference in the electrical potentials that the structures experience under the light excitation in the two measurement techniques. In the PV samples, the active layers are between two electrodes (ITO and InGa) and each charge is electrostatically attracted by the closer electrode. In the optical measurements, the film structures do not exhibit any electric field. In the photovoltage measurements, since the charge separation distance is proportional to the distance of the CS state from the electrodes, the polarization caused by the two electrodes should not be neglected. This has a consequence on the free energy of the CS state. According to our estimations, the variation in energy due to the electrode polarization is roughly 15 meV. The lower energy of the CS state in photoelectrical signals explains the higher stability and thus the longer lifetime of the electrical responses compared to the optical ones.

4.4 Photocurrent generation from photoelectrochemical cells

Learning to know the intra- and intermolecular photoinduced interactions between the studied molecules gave useful insights for the development of photovoltaic devices. The first step is to evaluate the PC generated by the investigated structures. For samples consisting exclusively of LB films, the only possible way to investigate the photovoltaic characteristics of the studied film systems was to build a three-electrode photoelectrochemical cell as described in Section 3.3.[I] In fact, being the LB films extremely thin and fragile, the evaporation of a solid electrode would destroy the underlying organic layers and eventually result in short circuit of the cell. Samples for PC measurements had similar structure as those used in the PV measurements except that the active layers were deposited directly on the ITO anode and no insulating ODA layers were deposited on top of the active layers.

4.4.1 Bilayers with PHT

The first series of samples herewith analyzed had the following general structure: ITO|**PHT**|X|electrolyte, where X represents either **V-79** or **PDI,** and the electrolyte composition is the one already given in Section 3.3. The steady-state PC measurements were carried out at the excitation wavelengths of 532 and 690 nm, where **PHT**, **PDI**, and **V-79** have their absorption maxima. The cells were illuminated with stepwise excitation, and the generated current was monitored as a function of time.

In Table 4.5, the full set of measured structures is shown, together with the main photovoltaic parameters derived from the PC experiments.

When **PHT** was coupled with **V-79**, an increase in the generated PC at the excitation wavelength of 532 was observed: from 3 nA/cm^2 for **PHT** alone, to roughly 45 nA/cm^2 for the **PHT**|2**V-79** structure, and to 300 nA/cm^2 for the **PHT**|6**V-79** configuration (Table 4.5). Hence, when the number of **V-79** increased, the cell performance enhanced.

Table 4.5 *Short circuit current (I_{SC}) from steady-state PC measurements, absorption (A), external (Φ_E) and internal (Φ_I) quantum yields of collected charges at different excitation wavelengths (λ_{exc}).*

Active layers	λ_{exc}, nm	I_{SC}, nA/cm^2	*A*	Φ_E, %	Φ_I, %
PHT|2 **V-79**	532	44.6	0.028	0.02	0.34
	690	17.0	0.016	0.01	0.28
PHT|6 **V-79**	532	299.2	0.031	0.14	2.00
	690	107.5	0.040	0.06	0.72
PHT|2 **PDI**	532	189.2	0.033	0.09	1.20
PHT|6 **PDI**	532	148.9	0.054	0.07	0.59
PHT	532	3	0.008	---	---

Samples containing **PDI** on the top of **PHT** showed a different behaviour. The highest PC, and thus the highest efficiency, was obtained for 2 **PDI** layers, but switching from 2 to 6 **PDI** layers, the PC was reduced. Moreover, a double **PDI** layer was more effective than a double **V-79** layer. The results are coherent with the photovoltage results of Section 4.3.1. In PV experiments the most efficient CT was obtained for **PDI** samples, and the effect of multilayered **V-79** on **PHT** was greater than that of the multilayered **PDI**. In Table 4.5, the quantum yields of collected charges are reported: the external quantum yield (Φ_E), which is defined as the fraction of incident photons converted to electrical current, and the internal quantum yield (Φ_I), which represents the fraction of absorbed photons converted to electrical current. The highest internal quantum yield reached in this series was 2 %, achieved with the **PHT**|6**V-79** structure at the excitation wavelength of 532 nm.

4.4.2 Multilayered structures with P–F

The introduction of **P–F** in the heart of the previously described **PHT**|**V-79**, **PDI** cells leads to multilayered structures with enhanced efficiency. A set of samples with generic structure **PHT**|**P–F** |X, with X equal to either **V-79** or **PDI** is presented in Table 4.6, together with the photovoltaic parameters obtained from the PC responses recorded at 430, 540, and 690 nm. A reference sample containing

only **PHT** and **P–F** was also measured to evaluate the influence of the secondary electron-acceptor. The well-known interlayer ET from **PHT** to **P–F**[18] promotes the PC generation, as a consequence of the preferred direction induced to the charges. In fact, the PC generated by the bilayered **PHT**|**P–F** cell is significantly higher than that produced by the structure containing **PHT** alone (Table 4.5).

Table 4.6 *Short circuit current (I_{SC}) from steady-state PC measurements, absorption (A), external (Φ_E) and internal (Φ_I) quantum yields at different excitation wavelengths (λ_{exc}).*

Active layers	λ_{exc}, nm	I_{SC}, nA/cm^2	*A*	Φ_E, %	Φ_I,, %
PHT|**P–F**	430	60.9	0.017	0.04	1.18
	540	50.0	0.025	0.02	0.42
	690	0.9	0.001	0.001	0.19
PHT|**P–F**|2 **V-79**	430	109.8	0.023	0.08	1.55
	540	177.1	0.029	0.09	1.34
	690	51.8	0.016	0.03	0.85
PHT|**P–F**|6 **V-79**	430	357.7	0.036	0.25	3.14
	540	466.2	0.024	0.21	3.99
	690	188.9	0.039	0.11	1.30
PHT|**P–F**|12**V-79**	430	434.4	0.02	0.31	6.85
	540	570.4	0.03	0.25	4.30
	690	365.0	0.04	0.21	2.41
PHT|**P–F**|2 **PDI**	430	442.5	0.020	0.29	6.54
	540	452.8	0.027	0.21	3.54
PHT|**P–F**|6 **PDI**	430	299.0	0.029	0.18	2.77
	540	326.0	0.046	0.12	1.15
PHT|**P–F**|12 **PDI**	430	63.0	0.035	0.04	0.45
	540	137.0	0.077	0.06	0.37

Moreover, when **V-79** or **PDI** was added to the **PHT**|**P–F** system, the generated PC was further increased. In Table 4.6, the thickness (or in other words the number of layers) of **V-79** or **PDI** was varied to optimize the quantum yield produced by the cells. For the samples containing **V-79**, by increasing the number of **V-79** layers the PC, and thus the quantum yield, always increased. The highest internal quantum yield, 7 %, was achieved at the dyad excitation wavelength (430 nm) for the structure containing 12 **V-79** layers. **P–F** plays a crucial role in these cells, since it

initiates the efficient multistep ET through the films. This explains why the best performance is obtained at 430 nm, where the dyad is mainly photoexcited.

In the **PDI**-sample series (**PHT**|**P–F**|**PDI**), the increase in the number of acceptor layers led to lower PC amplitudes. Efficiencies were dramatically reduced when switching from 2 to 12 **PDI** layers (Table 4.6). This is due to the low mobility of **PDI** films, whose thickness in the cells must be accurately optimized.

By comparing the performance of **V-79** and **PDI** cells, it is clear that **PDI** interacts more efficiently than **V-79** with **P–F** at the CS state ($\mathbf{P^{+}–F^{-}}$), as shown in PV experiments as well. The Φ_I of **PHT**|**P–F**|2**PDI** is 4 times higher (being 6.5 %) than that of the corresponding structure with **V-79** (1.6 %), assuming a similar interaction of **V-79** and **PDI** with MV^{2+} (being the LUMO levels of **V-79** and **PDI** very close to each other).

4.4.3 Structures including the PHT|ZnPH4 heterojunction

In this section, it is shown how to enhance the performance of the photovoltaic devices by applying the essential information obtainable from the ET studies. Recently, a vectorial photoinduced ET was demonstrated from **PHT** to the phthalocyanine derivative **ZnPH4**.[20] The two compounds originated a promising **PHT**|**ZnPH4** heterojunction for photovoltaic applications.[20] Multifunctional layered systems were here developed, by combining the system **P–F**|**V-79**, for which the CT was studied in Section 4.3.1, with the **PHT**|**ZnPH4** heterojunction.[I] The PC generated from a photoelectrochemical cell was evaluated by recording the *I–V* characteristics, from which the main photovoltaic parameters were derived. The most significant results are summarized in Table 4.7. The multilayer **PHT**|**ZnPH4**|**P–F**|**V-79** had better performance than the reference sample **PHT**|**ZnPH4**. The increase in the PC (and quantum yield) results from the vectorial multistep ET from **PHT** to **V-79**. In such a complex film structure, the lifetime of ET is prolonged as a consequence of the increased charge separation distance, and of the lateral diffusion of electrons in the acceptor layer. Moreover, the better performance can be attributed *i)* to the enhanced coverage of the solar spectrum in the multilayered structure, *ii)* to the polarization of neighbouring layers that support the ET, and/or *iii)* to additional energy transfer process which results in better light harvesting to obtain the ET state.

Table 4.7 *Short-circuit current (I_{SC}), open-circuit voltage (U_{OC}), fill factor (FF), absorption (A), external (Φ_E) and internal (Φ_I) quantum yields at different excitation wavelengths (λ_{exc}), as derived from I–V characteristics. The full sample structure is ITO|active layers|electrolyte.*

Active layers	λ_{exc}, nm	I_{SC}, μA/cm^2	U_{OC}, V	*FF*	*A*	Φ_E, %	Φ_I, %
PHT|ZnPH4	540	3.65	0.14	0.20	0.16	1.27	4.13
	705	1.89	0.13	0.22	0.09	0.91	4.85
PHT|ZnPH4|P–F|2 **V-79**	430	2.01	0.25	0.20	0.11	1.21	5.41
	540	4.03	0.25	0.22	0.15	1.40	4.79
	690	0.69	0.21	0.21	0.08	0.29	1.75
	705	0.67	0.23	0.21	0.10	0.32	1.54
PHT|ZnPH4|P–F|6 **V-79**	430	3.4	0.35	0.23	0.15	2.05	7.14
	540	4.4	0.35	0.22	0.17	1.52	4.80
	690	3.0	0.31	0.22	0.11	1.26	5.79
	705	3.2	0.33	0.21	0.12	1.59	6.41

The highest internal quantum yield (slightly over 7 % at 430 nm) was achieved by increasing the number of **V-79** layers up to 6 (cell structure: ITO|**PHT**|**ZnPH4**|**P–F**|6**V-79**|electrolyte). Similar tests were done with **PDI** replacing **V-79** in the devices, but the cells were less efficient than those with **V-79** films. An explanation for such behaviour can be identified in the low charge mobility of **PDI**, as discussed in [I].

4.5 Multilayered solar cells

The photoelectrochemical cells discussed in Section 4.4 are not reasonable for large scale applications. Their fabrication is not simple, and they require a careful sealing. Moreover, the electrolytic cells suffer of poor efficiencies and very low stability. The use of a solid electrode simplifies the cell preparation, and the resulting devices can potentially reach high efficiencies and stabilities. In this section, the fabrication and the characterization of multilayered solar cells with metal top-electrode is discussed. A novel strategy to increase the efficiency and stability of layered cells is presented.[IV,V] It is worth mentioning that the efficiencies obtained in this work are quite low, though comparable with those of similar unencapsulated layered cells in air presented in literature.[197–199] However, the main contribution of this study is to offer a strategy that can be further applied to more efficient devices.

4.5.1 The organics|top-electrode junction

A good electrical contact between the active layers and the top-electrode has to be ensured for the correct functioning of the solar cells. Since very thin photoactive films are used, it is essential that the electrode deposition does not damage the underlying layers, so as to avoid short-circuiting problems.

A promising strategy to optimize the organics|top-electrode junction, based on the introduction of a thin **Alq$_3$** buffer layer at the interface between the organics and an Au cathode is presented here.[IV] The influence of the **Alq$_3$** introduction on the efficiency and the lifetime of the photovoltaic cells is also discussed.

Since the chemical degradation of electrodes has a strong impact on the device lifetime, we have adopted Au as metal electrode due to its high stability in oxidizing environment.

To test the effect of **Alq$_3$**, we have selected a well-known bilayered cell based on the **CuPc|C$_{60}$** heterojunction, being easy to make and to be compared with other published works. Two devices were built, one containing **Alq$_3$** and another one not containing it, referred to in the following as **Alq$_3$**-cell and reference-cell, respectively. The structures of the measured samples, together with the photovoltaic parameters derived from the *I–V* characteristics, are presented in Table 4.8. The *I–V* curves were recorded in dark and upon 1000 W/m^2 white light illumination, as shown in Figure 4.10. The **Alq$_3$**-cell (ITO|**CuPc**|**C$_{60}$**|**Alq$_3$**|Au) clearly shows a better performance than the reference-cell (ITO|**CuPc**|**C$_{60}$**|Au): the I_{SC} is roughly 9 times higher, the U_{OC} is enhanced 4 times, and the *FF* is doubled.

Table 4.8 *Photovoltaic parameters for the measured devices obtained from the I–V characteristics.*

Active layers	I_{SC}, mA/cm^2	U_{OC}, V	*FF*	η, %
CuPc|C$_{60}$	0.6	0.07	0.22	0.01
CuPc|C$_{60}$|Alq$_3$	5.0	0.28	0.40	0.60

For the **Alq$_3$**-cell, the η-value is increased 60 times. Such a big difference between the two devices could be explained by the effect that **Alq$_3$** buffer layer has on the Au electrode. When Au is evaporated on the top of **Alq$_3$**, it can merge with the **Alq$_3$** layer, thus resulting in a lower cathode work function. Similar characteristics of the **Alq$_3$**|Au interface that supported the proposed mechanism have been reported earlier,[200,201] mainly with respect to OLEDs. In both devices, electrons are moving

from ITO towards Au (and/or holes are moving in the opposite direction). The lowering of the Au work function due to the presence of **Alq_3** could facilitate the electron movement due to the reduced difference between ITO and Au work functions. Another possible reason for the improved performance of the **Alq_3**-cell with respect to the reference-cell lies in the blocking effect of **Alq_3** on the diffusion of cathode atoms into the active layer during the deposition, as proposed by Song *et al.*[156] The evaporation of Au can damage the surface due to the formation of clusters of atoms. The **Alq_3** buffer layer can thus significantly improve the efficiency of the cell by protecting the **C_{60}** layer.

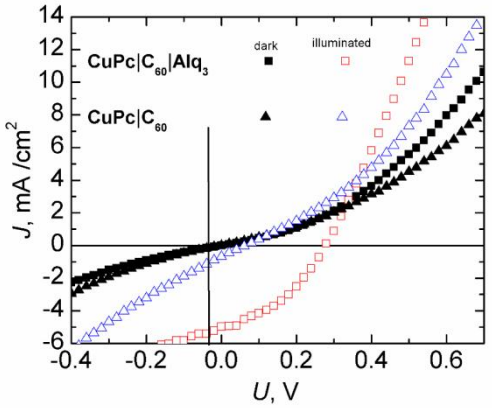

Figure 4.10 *Current density (J) vs. voltage (U) characteristics of the studied devices upon 1000 W/m^2 simulated AM 1.5 solar illumination.*

Degradation of the **Alq_3**-cells in time, when exposed to air without encapsulation was analyzed in detail. A cell having exactly the same structure as the one described above (ITO|**CuPc**|**C_{60}**|**Alq_3**|Au) was prepared and measured immediately after its preparation, and for a whole period of 18 weeks. It must be underlined that a small discrepancy exists in the performance of the device at t = 0 (as taken from vacuum) with respect to the data of Table 4.8. In fact, for this cell I_{SC}, U_{OC}, *FF*, and η are 3.6 mA/cm^2, 0.32 V, 0.41 %, and 0.47 %, respectively. The slightly worse performance of the cell can be attributed to the uncertainty in the active layer thicknesses. The degradation of such device in air is presented in Figure 4.11. In addition to η, its constituents (I_{SC}, U_{OC}, *FF*) are also depicted in Figure 4.11 in order to evaluate the main reason for the degradation. All the photovoltaic characteristics are normalized to their initial values and plotted as a function of exposure time to air in the dark. The main degradation occurs in the first hours and proceeds slowly. During the first hour, η decreases about 28 %. This degradation is partly attributed to the fast

decrease in I_{SC} and partly to that of *FF*. Open-circuit voltage does not vary over time and remains constant during the whole experiment (18 weeks). Stability of U_{OC} can be attributed to the presence of **Alq$_3$**, confirming what was previously observed by varying several ETLs in the cell.[156] I_{SC}, *FF*, and η decay nearly exponentially with time. The half-lifetime of the device, defined as the degradation time of η from the initial value to half of it, is over 7 weeks. After 18 weeks the solar cell has 30 % of its efficiency left.

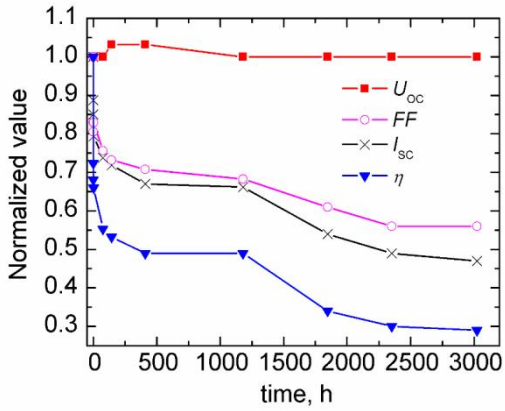

Figure 4.11 *Degradation of the ITO|**CuPc**|**C$_{60}$**|**Alq$_3$**|Au device in air. Normalized I_{SC}, U_{OC}, FF, and η vs. time.*

It is worth noting that all devices were simply stored in a dark environment at ambient conditions. Nonetheless, they survived for a long time. The use of Au cathode in the cell leads to a much longer lifetime compared to that of a similar cell with Al as top-electrode. Song *et al.* have published a half-lifetime of 61 h for an Al cathode cell with the same active layer structure.[156] Hence, we can conclude that the use of Au as top-electrode in our devices is the main responsible for the achievement of stable cells.

4.5.2 D–A pair in layered solar cells

The final goal of our research has been the development of multilayered organic photovoltaic cells, where each layer is responsible for an individual function. After the first step in this direction has been accomplished by optimizing the junction between organics and metal electrode, the next challenge is devoted to the active layers of the cells, which are selected and assembled according to the directions obtained from the ET studies.

The heart of our multilayered cell is the D–A pair, which is sandwiched between an additional donor (HTL) and acceptor (ETL) layers (see Chart 4.4). To the best of our knowledge, it is the first time that such cell scheme is proposed.

The primary photoinduced CS, which is the first step of the consecutive interlayer ET processes, takes place at the D–A interface. The cell scheme resembles the idea of the multistep ET, occurring through several donors and acceptors, which can contribute to a CS state where charges are separated by a long distance, thus retarding the undesired back electron transfer.

The novel double-bridged phthalocyanine-fullerene dyad, **H_2Pc–C_{60}ee**, was successfully tested in layered cells as a spin-coated film between a donor (**PHT**) and an acceptor layer (**PTCDI** or **C_{60}**).[V] Its contribution to the efficiency of the device, and its role in the cell is hereby discussed.

A set of five solar cells, whose structures are explicated in Table 4.9, was measured to this aim.

Table 4.9 *Photovoltaic parameters for the studied devices obtained from the I–V characteristics.*

Active layers	I_{SC}, mA/cm^2	U_{OC}, V	*FF*	η, %
PHT|PTCDI	0.69	0.25	0.35	0.12
PHT|H_2Pc–C_{60}ee|PTCDI	1.15	0.45	0.28	0.32
PHT|C_{60}	1.14	0.21	0.35	0.18
PHT|H_2Pc–C_{60}ee|C_{60}	0.93	0.50	0.34	0.30
PHT:H_2Pc–C_{60}ee|PTCDI	2.50	0.33	0.24	0.40

I–V characteristics of the fabricated devices, in dark and under white light illumination of 532 W/m^2, are shown in Figure 4.12. All the samples present a good diode behaviour in the dark. When illuminated, the devices containing the dyad layer exhibit better performances than the samples not containing the dyad. The main photovoltaic parameters derived from the *I–V* curves are summarized in Table 4.9.

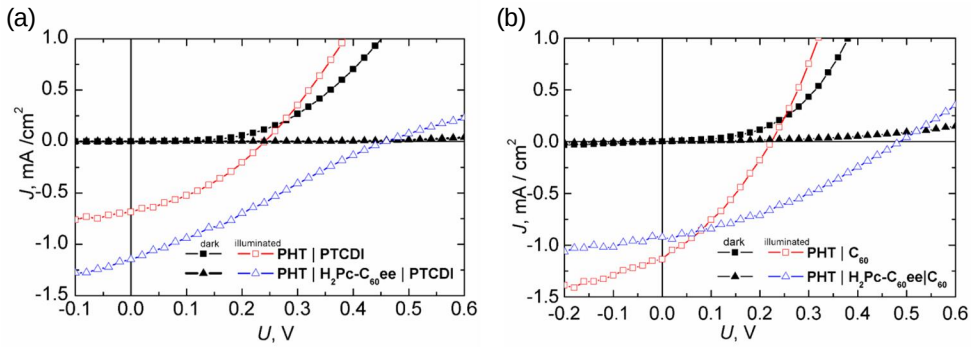

Figure 4.12 *Current (J) vs. voltage (U) characteristics in dark and under 532 W/m^2 simulated AM 1.5 solar illumination for the* ***PTCDI****-cells (a) and* ***C_{60}****-cells (b).*

As regards the devices containing **PTCDI** (Figure 4.12a), the dyad sample produces a current of 1.15 mA/cm^2 under illumination, while the reference cell (**PHT**|**PTCDI**) generates only 0.69 mA/cm^2. In spite of its lower absorbance in the 500–600 nm wavelength range of the spectrum, the cell containing **H_2Pc–C_{60}ee** produces higher current. This is mainly due to the significant absorption of the dyad at 700 nm, which widens the absorption spectrum of the dyad sample compared to the reference, and allows it to better match the solar emission spectrum. However, this cannot be the only reason for the enhanced photocurrent, since the absorbance is quite low at 700 nm (around 0.1). The main reason for higher current lies in the facilitated electron movement from **PHT** to **PTCDI** through the dyad layer. In fact, the introduction of **H_2Pc–C_{60}ee** results in two different junctions in the cell (**PHT**|**H_2Pc–C_{60}ee** and **H_2Pc–C_{60}ee**|**PTCDI**) instead of the one in **PHT**|**PTCDI**. The D–A pair acts as a charge-sorting layer, thus contributing to a more efficient charge transport towards the electrodes.

As regards the samples containing **C_{60}** as acceptor layer, a different behaviour is found. In this case, the photocurrent of the reference cell is higher than that of the dyad sample. This can be explained by the fact that electrons are not so efficiently transferred from the fullerene moiety of the dyad to another fullerene layer (evaporated on top of it), but rather they are easily transported from **PHT** to **C_{60}**.

For all the four analyzed solar cells, a clear increase in the open-circuit voltage is achieved due to the introduction of the dyad. This has the biggest impact on the enhancement of the power conversion efficiency. In the **PTCDI**-series, the η-value was increased by almost three times in the dyad cell compared to the reference (from 0.12 % up to 0.32 %). In **C_{60}**-containing cells, η of the dyad sample (being

0.30 %) was more than one and a half times higher than that of the reference in absence of the dyad (0.18 %). It must be emphasized that in these experiments the device fabrication is not yet optimized, especially in terms of the cell active layers thickness. We believe that this is the main reason for the limited performances of the devices.

In order to understand the origin of the enhanced U_{OC} in the dyad samples, the role of the D–A pair in the cell should be described. A multistep ET is expected to occur in a multilayered system. The primary ET process takes place from the phthalocyanine moiety (yielding a cation) to the fullerene (yielding an anion). The **PHT** layer acts as antenna layer and secondary electron donor, which provides electrons to the dyad. **PTCDI** and **C_{60}** behave as secondary electron acceptors, taking electrons from the fullerene anion of the dyad, and at the same time as electron transporting layers. After electrons are transported to the last ETL layer, *i.e.*, **Alq_3**, they are collected at the cathode. The main contribution to the charge separation is given by the D–A pair, thus being responsible for the generated additional voltage with respect to the reference sample.

The **PTCDI** containing samples were also tested with monochromatic light, by recording the *I–V* curves at the excitation wavelengths of 518, 540, 582, and 700 nm where the maxima in the absorption spectra lie. The photovoltaic parameters derived from the *I–V* characteristics are summarized in Table 4.10.

Table 4.10 *Photovoltaic parameters and quantum yields for the* ***PTCDI****-cells obtained from the I–V characteristics under monochromatic illumination.*

Active layers	λ_{exc}, nm	I_{SC}, nA/cm^2	U_{OC}, V	*FF*	Φ_E, %	Φ_I, %
PHT|PTCDI	518	51.9	0.21	0.47	3.86	6.72
	540	57.5	0.21	0.48	4.19	7.85
	582	64.9	0.23	0.45	4.37	8.64
	700	0.25	0.05	0.26	0.02	0.56
PHT|H_2Pc–C_{60}ee|PTCDI	518	46.3	0.31	0.29	3.44	5.93
	540	51.0	0.33	0.28	3.72	6.91
	582	63.4	0.35	0.28	4.27	8.23
	700	12.8	0.25	0.31	0.98	5.18

At the wavelengths where **PHT** and **PTCDI** mainly absorb, the reference generates slightly higher photocurrent, and thus higher quantum yields are achieved. The U_{OC} is always higher for the dyad sample, while the *FF* is decreased. At 700 nm, the dyad sample exhibits over 50 times higher I_{SC} than the reference; a corresponding huge increase in the quantum yield can be observed as well.

The reduction in the absorption, and consequently in the generated photocurrent, in the central part of the spectrum due to technical reasons in the film preparation (as mentioned in Section 4.2.1) is the main reason for reduced efficiencies. In order to avoid the partial washing of the **PHT** layer caused by the dyad deposition, a mixed solution of **PHT** and **H_2Pc–C_{60}ee** is proposed for the spin-coating. The most appropriate solvent was selected according to the solubility of both compounds, and thus chloroform was chosen. The resulting 1:1 mass mixture **PHT**:**H_2Pc–C_{60}ee** (with concentration 3 g/l) was then spin-coated, and the evaporated ETLs were deposited on top of it, before the Au evaporation. The results from the photocurrent measurements under white-light illumination are reported in Table 4.9. The sample with mixed **PHT**:**H_2Pc–C_{60}ee** layer has the best performance among all the other cells with **H_2Pc–C_{60}ee** dyad. This result is explained by the wider absorption of the sample, which now significantly absorbs in the 500–600 nm wavelength range as well.

Although showing promising results, the solar cells based on the spin-coated **H_2Pc–C_{60}ee** dyad can be significantly improved. The main problem of such cells lies in that the dyad layer is unoriented (being spin-coated), and thus the ET does not proceed in one defined direction throughout the whole film structure. If a system with molecularly oriented films would be built, a more efficient ET and thus a more efficient CS would be achieved, and this would have a consequence on the efficiency of the collected charges as well. Porphyrin-fullerene dyads have been extensively used in [I–III] as oriented systems for performing vectorial ET. Thus, the next challenge would be to build up a multilayered solar cell with oriented molecular films.

An example is shown in [II], where the information about the intra- and intermolecular photoinduced interaction between **P–F** and **PTCDI** gained from the ET studies is used to build a layered cell. The cell contains **P–F** and **PTCDI** as active layers, with the addition of an **Alq_3** buffer layer before the Au cathode evaporation. The *I–V* curves for the **P–F**|**PTCDI** cell and for a reference cell containing only **PTCDI** are shown in Figure 4.13a. **PTCDI** cell is constituted by a single non-oriented layer with high resistance. Its *I–V* characteristics show a nearly Ohmic behaviour, typical for photoresistors. When **P–F** is coupled with **PTCDI**, the *I–V* curve of the bilayered cell has a totally different shape, which resembles that of a photodiode. Moreover, the bilayered cell generates distinctive photocurrent and shows reasonable U_{OC} under illumination, which allows it to produce electrical power. Clearly, a preferred direction for electrons is induced in the bilayer structure

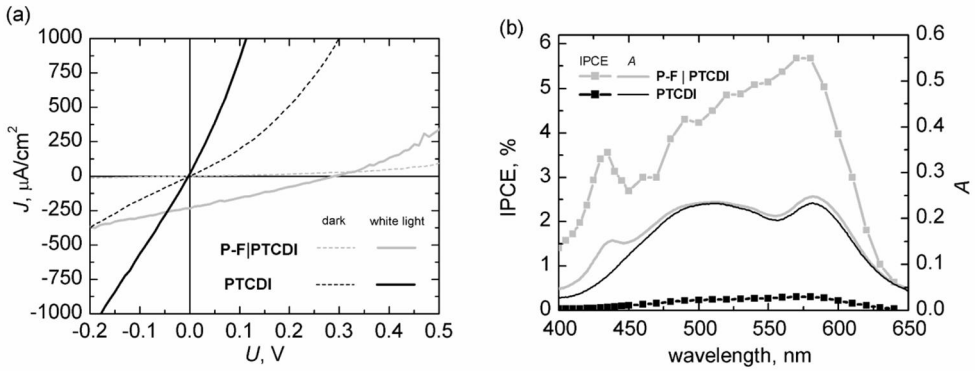

Figure 4.13 *Current (J) vs. voltage (U) characteristics in darkness and under 532 W/m^2 simulated AM 1.5 solar illumination (a), and IPCE and absorption spectra (b) of* ***P–F|PTCDI*** *and* ***PTCDI*** *structures.*

as a consequence of the ET, and the separated charges are collected at the respective electrodes resulting in generated photocurrent.

Action (IPCE) spectra of the two samples are presented in Figure 4.13b. Both of them resemble the shape of the respective absorption spectra, showing that the generated photocurrent results from the absorption.

The introduction of dyad is crucial to the enhanced photocurrent generation of the bilayered cell, since the **PTCDI** single layer cell has an extremely low IPCE. The contribution of **P–F** to the photocurrent is evident from the pronounced peak at 430 nm, which corresponds to the dyad absorption maximum. However, the action spectrum of **P–F|PTCDI** shows that the main contribution to the photocurrent comes from the wavelength region where **PTCDI** absorbs (above 500 nm). For a more quantitative analysis, the photovoltaic parameters calculated from the action spectra are given in Table 4.11. The highest internal quantum yield (being 13 %), calculated from the action spectra, is achieved by **P–F|PTCDI** at both 430 and 580 nm. The system needs improvements though, mainly to enhance the absorption of the films and the coverage of the solar spectrum.

Table 4.11 *Short circuit current (I_{SC}) from PC measurements, absorption (A), external (Φ_E) and internal (Φ_I) quantum yields at different excitation wavelengths (λ_{exc}). The full sample structure is ITO|active layers|**Alq$_3$**|Au.*

Active layers	λ_{exc}, nm	I_{sc}, μA/cm^2	*A*	Φ_E, %	Φ_I, %
P–F|PTCDI	430	4.38	0.132	3.41	13.0
	510	6.05	0.235	4.50	10.7
	580	4.39	0.247	5.67	13.1
PTCDI	430	0.08	0.066	0.06	0.4
	510	0.32	0.226	0.24	0.6
	580	0.24	0.224	0.31	0.7

Preliminary attempts of building more complex devices, whose active layers resemble the configurations of the ET studies[III], have been discussed in [III].

The long lifetime of the charge separation in the **PHT**|**P–F**|**PTCDI** multilayer makes this structure a potential candidate for OPVs. Early experiments have been carried out, and the results are briefly reported in [III]. When the PC generation was tested in a three-electrode photoelectrochemical cell, a significantly better performance was achieved in the **PHT**|**P–F**|**PTCDI** trilayer sample compared to the **PHT**|**PTCDI** bilayer, thus proving the key contribution of the dyad to the enhancement of the PC by increasing the lifetime of the charge separation.

However, when solar cells having same active layers but with **Alq$_3$**|Au cathode were built, a smaller PC was generated from the trilayer structure with respect to that produced by the **PHT**|**PTCDI** bilayer.[III] The reasons for such behaviour are not yet clear. It is possible that the **P–F** film undergoes some structural changes during the cathode evaporation, which has consequences on the junction between **P–F** and **PHT**. Further research is required to explain such results, and to optimize each junction in the photovoltaic devices.

4.6 Future perspectives for organic photovoltaics

The results achieved with this work provide a relevant step towards the understanding of the photophysics of thin film systems for photovoltaic applications. Moreover, our first attempts to build devices for energy conversion can pave the way for the development of layered solar cells. Nevertheless, few issues are still left open, mainly concerning the performance of the fabricated photovoltaic devices.

The highest power conversion efficiency presented in this work was 0.60 % for an ITO|**CuPc**|**C_{60}**|**Alq_3**|Au cell.[IV] Such a low efficiency value lies in the average range of performances typically obtainable with unencapsulated layered solar cells in air. It must be underlined that the aim of this study was to offer a novel strategy based on the multistep ET that can be applied further to more efficient devices, and not to focus on the achievement of competitive efficiencies.

In this section, the main weaknesses of our solar cells are discussed, and an outlook to suggested future research to achieve more efficient devices is given.

The main reason for the poor performance of the discussed layered systems is their low total absorption. In the best case, the absorbance of the cell was below 0.3.[V] Unfortunately, the layers thickness could not be freely increased to achieve higher absorption due to the low charge transport mobility of organic semiconductors. In fact, thicker devices present also larger series resistances and a higher possibility that generated charge carriers will recombine before they reach their respective collecting electrodes.[207] In our studies the optimization of the active layers thickness was not at all considered yet.

Another problem of the presented device is the limited spectral range of absorption, which cause a mismatch between the absorption spectrum of the photoactive materials and the terrestrial solar spectrum. In other words, a large part of the solar irradiation is not used for the light-to-current conversion. One way to overcome this problem could be to use, in the same device, different organic materials with complementary absorption spectra, so as to increase the photon harvesting. Interesting compounds used to enhance the light harvesting are the so-called low-bandgap materials. Typical dyes for organic solar cells harvest mainly the blue, green, and yellow parts of the solar spectrum. The low energy gap materials absorb in the red and infrared parts of the spectrum. The introduction in the cells of antenna systems of absorber materials that donate the energy absorbed in the blue/green part of the spectrum to the red absorbing solar cell materials represents a promising way to enhance the efficiency.[208]

The central layer of our cells is the D–A pair, which showed a crucial role in initiating the multistep ET of the analyzed film configurations. However, its introduction in solar cells leads to many open questions.

The porphyrin-fullerene dyad has been mainly used in this Thesis for the ET studies, since it is an efficient and highly oriented system. The optical density of a **P–F** monolayer is extremely low. The dyad absorption spectrum shows a narrow peak centered at 430 nm. The limited absorption of porphyrin-fullerene dyads can be overcome by replacing these compounds with the phthalocyanine-fullerene

dyads, whose absorption spectrum better overlaps with that of the sun. For this reason, in [V] the **H_2Pc–C_{60}ee** dyad was used. Nevertheless, such molecule does not clearly orient on the surface as porphyrin-fullerene dyads do. A new phthalocyanine-fullerene dyad has been very recently synthesized,[209] which is expected to allow combining the advantage of the orientation of **P–F**, with the wider absorption of **H_2Pc–C_{60}ee**.

New deposition techniques for the dyad in solar cells should be also investigated. When **P–F** was deposited in multilayered cells (as mentioned in [III]), it showed worse performance than a reference cell not containing the dyad and this was attributed to the effect of the metal evaporation on the LB/LS films of **P–F**, and especially on the junction between the donor layer (**PHT** in the reported example) and **P–F**. The LB/LS have the advantage of being relatively simple and cheap methods for layer-by-layer assembling of molecular structures. However, these films are very fragile and thin, and thus they can easily degrade or get damaged during the solar cell fabrication. The self-assembly technique, though challenging from the synthetic point of view, could be a solution for successful deposition of oriented dyads in solar cells.

Finally, the low open-circuit voltage (0.3–0.5 V in the best cases) of the presented devices should be considered as another reason for their poor performance. In layered cells, the U_{OC} is strongly dependent on the difference between the HOMO and LUMO levels of donor and acceptor. The electrode work functions do not have a great influence on the U_{OC}, as seen in the comparisons with Al-cathode cells presented in [IV,V].

In order to increase the U_{OC} of the cells, new donor and acceptors materials with better matching electronic bandgaps should be investigated. Furthermore, performing a serial connection between unit cells (tandem approach) can be a viable strategy to increase the U_{OC}.

5 Conclusions

The main results of this Thesis can be summarized as follows:

1. The capability of different *n*-type materials (**V-79**, **PDI**, **PTCDI**) to act as secondary electron-acceptors with respect to the **P–F** dyad was demonstrated. In all the cases, an efficient intermolecular ET from the photoinduced fullerene anion of **P–F** to the mentioned compounds took place, as shown by photoelectrical and spectroscopic techniques. The most efficient bilayer was the couple **P–F**|**PTCDI**. Strong photoelectrical signals were achieved, mainly due to the enhancement in the film preparation technology. For the film deposition, the LB technique was replaced by the LS and thermal evaporation methods, thus leading to smooth films containing 100 mol % of active molecules. This enhanced the coverage of active molecules in the films compared to the previously studied systems. In the **P–F**|**PTCDI** system, the final transient **P**$^{+}$**–F**|**PTCDI**$^{-}$ state was found at both the excitation wavelengths of **P–F** and **PTCDI**, as demonstrated by the PV measurements and supported by the laser flash-photolysis measurements. Different mechanisms were proposed depending on the moiety that is photoexcited.

2. The study of ET was extended to more complex layered systems, consisting of HTL, D–A pair, and ETL. A multistep ET took place through the films, as investigated by the photovoltage and laser flash-photolysis techniques. **PHT** was used as HTL, while **P–F** and **PTCDI** as D–A pair and ETL, respectively. After the primary ET in **P–F**, secondary processes included ET from **PHT** to porphyrin cation of **P–F**, and from the fullerene anion to **PTCDI**. The final transient states corresponding to **PHT** cations and **PTCDI** anions were found for the **PHT**|**P–F**|**PTCDI** structure (**PHT**$^{+}$|**P–F**|**PTCDI**$^{-}$). The introduction of **PHT** into the structures was responsible for a significant increase in the amplitude and lifetime of both PV and flash-photolysis signals. The longer-lived CS in the multilayers containing **PHT** represents indeed an advantage when thinking about photovoltaic devices.

3. The essential information obtained from the ET studies was used to build structures for photovoltaic applications. To prove the photocurrent generation

from ultrathin film systems, a three-electrode photoelectrochemical cell was built.

4. In order to develop layered cells with a metal top-cathode, the optimization of the organics|top-electrode junction was crucial. This was achieved with the introduction of an **Alq_3** buffer layer between the top most organic layer and the cathode. **Alq_3** showed to bring significant improvements to the devices in terms of efficiency and lifetime. A relatively long lifetime organic solar cell in air, containing a thin **Alq_3** layer under an Au cathode was developed. It exhibited a η = 0.6 % and a half-lifetime of over 7 weeks. Moreover, an efficiency of 30 % of the initial value was found after 18 weeks.

5. The key role of the D–A pair in the heart of multilayered Au-cathode cells was demonstrated. A phthalocyanine-fullerene dyad (**$H_2Pc–C_{60}ee$**) was used as spin-coated D–A film, **PHT** as electron-donor, and **PTCDI** or **C_{60}** as acceptor. The introduction of **$H_2Pc–C_{60}ee$** led to a three times or one and half times higher efficiency compared to the reference cell (not containing the dyad) for the **PTCDI** or **C_{60}** cells, respectively. The main reason for such an enhancement was the increase in the open-circuit voltage, and the widening of the absorption spectrum of the sample when the dyad was added, which contributed to a better matching with the solar spectrum. Next logical step will be the introduction of oriented porphyrin- and phthalocyanine-fullerene dyads in the layered cells, and the optimization of each layer/junction in the devices in order to improve their efficiency.

6 References

1. *BP Statistical Review of World Energy June 2010*, Beyond Petroleum (BP), June 2010, http://www.bp.com/liveassets/bp_internet/globalbp/globalbp_uk_english/reports_and_publications/statistical_energy_review_2008/STAGING/local_assets/2010_downloads/statistical_review_of_world_energy_full_report_2010.pdf.
2. Kamat, P. V. *J. Phys.Chem. C* **2007,** *111*, 2834.
3. *Basic Research Needs for Solar Energy Utilization, Report on the Basic Energy Sciences Workshop on Solar Energy* Utilization, The U.S. Department of Energy (DOE) Office of Basic Energy Sciences, April 18–21, 2005, http://www.er.doe.gov/bes/reports/files/SEU_rpt.pdf.
4. Sun, S-S; Sariciftci, N. S. *Organic Photovoltaics: Mechanisms, Materials, and Devices*, CRC (Taylor & Francis group), **2005**.
5. Kuciauskas, D.; Lin, S.; Seely, G. R.; Moore, A. L.; Gust, D.; Drovetskaya, T.; Reed, C. A.; Boyd, P. D.W. *J. Phys. Chem.***1996**, *100*, 15926.
6. Imahori, H.; Fukuzumi, S. *Adv. Funct. Mater.* **2004**, *14*, 525.
7. Kesti, T. J.; Tkachenko, N. V.; Vehmanen, V.; Yamada, H.; Imahori, H.; Fukuzumi, S.; Lemmetyinen, H. *J. Am. Chem. Soc.* **2002**, *124*, 8067.
8. D'Souza, F.; Chitta, R.; Gadde, S.; McCarty, A. L.; Karr, P. A.; Zandler, M. E.; Sandanayaka, A. S. D.; Araki, Y.; Ito, O. *J. Phys. Chem. B* **2006**, *110*¸ 5905.
9. Imahori, H.; Sakata, Y. *Eur. J. Org. Chem.* **1999**, *1999*, 2445.
10. Gust, D.; Moore, T. A.; Moore, A. L. *Acc. Chem. Res.* **2001**, *34*, 40.
11. Hasobe, T.; Kamat, P. V.; Absalom, M. A.; Kashiwagi, Y.; Sly, J.; Crossley, M. J.; Hosomizu, K.; Imahori, H.; Fukuzumi, S. *J. Phys. Chem. B* **2004**, *108*, 12865.
12. Fukuzumi, S.; Imahori, H.; Yamada, H.; El-Khouly, M. E.; Fujitsuka, M.; Ito, O.; Guldi, D. M. *J. Am. Chem. Soc.* **2001**, *123*, 2571.
13. Imahori, H.; Guldi, D. M.; Tamaki, K.; Yoshida, Y.; Luo, C.; Sakata, Y.; Fukuzumi, S. *J. Am. Chem. Soc.* **2001**, *123*, 6617.
14. Vehmanen, V.; Tkachenko, N. V.; Tauber, A. Y.; Hynninen, P. H.; Lemmetyinen, H. *Chem. Phys. Lett.* **2001**, *345*, 213.

15. Mataga, N.; Chrosrowjan, H.; Taniguchi, S. *J. Photochem. Photobiol. C* **2005**, *6*, 37.
16. Liddell, P. A.; Kuciauskas, D.; Sumida, J. P.; Nash, B.; Nguyen, D.; Moore, A. L.; Moore, T. A.; Gust, D. *J. Am. Chem. Soc.* **1997**, *119*, 1400.
17. Peeters, E.; van Hal, P. A.; Knol, J.; Brabec, C. J.; Sariciftci, N. S.; Hummelen, J. C.; Janssen, R. A. J. *J. Phys. Chem. B* **2000**, *104*, 10174.
18. Vuorinen, T.; Kaunisto, K.; Tkachenko, N. V.; Efimov, A.; Lemmetyinen, H. *J. Photochem. Photobiol. A* **2006**, *178*, 185.
19. Kaunisto, K.; Vuorinen, T.; Vahasalo, H.; Chukharev, V.; Tkachenko, N. V.; Tolkki, A.; Lehtivuori, H.; Lemmetyinen, H. *J. Phys. Chem. C* **2008**, *112*, 10256.
20. Kaunisto, K.; Vahasalo, H.; Chukharev, V.; Tkachenko, N. V.; Vivo, P.; Niemi, M.; Tolkki, A.; Efimov, A.; Lemmetyinen, H. *Thin Solid Films* **2009**, *517*, 2988.
21. Kaunisto, K.; Chukharev, V.; Tkachenko, N. V.; Efimov, A.; Lemmetyinen, H. *J. Phys. Chem. C* **2009**, *113*, 3819.
22. Hu, X.; Schulten, K. *Phys. Today* **1997**, *50*, 28.
23. Koeppe, R.; Sariciftci, N. S. *Photochem. Photobiol. Sci.* **2006**, *5*, 1122.
24. Rice, M. J.; Gartstein, Y. N. *Phys. Rev. B* **1996**, *53*, 10764.
25. Beckers, E. H. A.; Meskers, S. C. J.; Schenning, P. H. J.; Chen, Z. J.; Wurthner, F.; Marsal, P.; Beljonne, D.; Cornil, J.; Janssen, R. A. *J. Am. Chem. Soc.* **2006**, *128*(2), 649.
26. Paddon-Row, M. N. *Acc. Chem. Res.* **1994**, *27*, 18.
27. Marcus, R. A. *Rev. Mod. Phys.* **1993**, *65*, 599.
28. Bolton, J. R.; Archer, M. D. *Adv. Chem. Ser.* **1991**, *228*, 7.
29. Jortner, J. *J. Phys. Chem.* **1976**, *64*, 4860.
30. Allemand, P. M.; Koch, A.; Wudl, F.; Rubin, Y.; Diederich, F.; Alvarez, M. M.; Anz, S. J.; Whetten, R. L. *J. Am. Chem. Soc.* **1991**, *113*, 1050.
31. Becquerel, E. *Comptes Rendus* **1839**, *9*, 561.
32. Borisenko, V. E.; Ossicini, S. *What is what in the Nanoworld: A Handbook on Nanoscience and Nanotechnology*, Wiley-VCH, **2008**.
33. Chapin, D. M.; Fuller, C. S.; Pearson, G. L. *J. Appl. Phys.* **1954**, *25*, 676.
34. Zhao, J.; Wang, A.; Green, M. A. *Sol. Energy Mater. Sol. Cells* **2001**, *66*, 27.

35. Geisz, J. F.; Friedman, D. J.; Ward, J. S.; Duda, A.; Olavarria, W. J.; Moriarty, T. E.; Kiehl, J. T.; Romero, M. J.; Norman, A. G.; Jones, K. M. *Appl. Phys. Lett.* **2008**, *93*, 123505.
36. *World Record: 41.1 % efficiency reached for multi-junction solar cells at Fraunhofer ISE*, Fraunhofer Institut Solare Energiesysteme (ISE), January 14, 2009, http://www.ise.fraunhofer.de/press-and-media/pdfs-zu-presseinfos-englisch/2009/press-release-world-record-41.1-efficiency-reached-for-multi-junction-solar-cells-at-fraunhofer-ise-pdf-file.
37. *UD-led team sets solar cell record, joins DuPont on $100 million project*, University of Delaware (UD), July 23, 2007, http://www.udel.edu/PR/UDaily/2008/jul/solar072307.html.
38. Tao, M. *The Electrochemical Society Interface* **2008**, *17*, 30.
39. Schultz, O.; Mette, A.; Preu, R.; Glunz, S. W. *Proceedings of the 22nd European Photovoltaic Conference and Exhibition*, Milano 2007.
40. Hegedus, S. *Prog. Photovoltaics Res. Appl*. **2006**, *14*, 393.
41. Dimroth, F. *Phys. Stat. Sol*. **2006**, *3*, 373.
42. Hagfeltd, A.; Grätzel, M. *Acc. Chem. Res.* **2000**, *33* (5), 269.
43. Grätzel, M. *Inorg. Chem.* **2005**, *44*, 6841.
44. Chen, C. Y.; Wang, M.; Li, J.-Y.; Pootrakulchote, N.; Alibabaei, L.; Ngoc-le, C.; Decoppet, J.-D.; Tsai, J.-H.; Grätzel, C.; Wu, C.-G.; Zakeeruddin, S. M.; Grätzel, M. *ACS Nano* **2009**, *3*, 3103.
45. Kato, T.; Okazaki, A.; Hayase, S. *Chem. Commun*. **2005**, 363.
46. Chamberlain, G. A. *Solar Cells* **1983**, *8*, 47.
47. Wöhrle, D.; Meissner, D. *Adv. Mater.* **1991**, *3*, 129.
48. Brabec, C. J.; Sariciftci, N. S.; Hummelen, J. C. *Adv. Funct. Mater*. **2001**, *11*, 15.
49. Nunzi, J-M. *C. R. Physique* **2002**, *3*, 523.
50. Liang, Y.; Xu, Z.; Xia, J.; Tsai, S.-T.; Wu, Y.; Li, G.; Ray, C.; Yu, L. *Adv. Mater.* 2010, **22**, E135.
51. *Solarmer breaks organic solar PV cell conversion efficiency record, hits NREL-certified 7.9 %*, Tom Cheyney, December 02, 2009, http://www.pvtech.org/news/_a/solarmer_breaks_organic_solar_pv_cell_conversion_efficiency_record_hits_nre.
52. *Konarka Power Plastic® Applications*, Konarka, 2010, http://www.konarka.com/media/pdf/konarka_market_overview.pdf.

53. Kim, J. Y.; Lee, K.; Coates, N. E.; Moses, D.; Nguyen, T.; Dante, M.; Heeger, A. J. *Science* **2007**, *317*, 222.
54. Ameri, T.; Dennler, G.; Lungenschmied, C.; Brabec, C. J. *Energy Environ. Sci.* **2009**, *2*, 347.
55. Hauch, J. A.; Schilinsky, P.; Choulis, S. A.; Childers, R.; Biele, M.; Brabec, C. J. *Sol. Energy Mater. Sol. Cells* **2008**, 92, 727.
56. Katz, E. A.; Gevorgyan, S.; Orynbayev, M. S.; Krebs, F. C. *Eur. Phys. J. Appl. Phys.* **2007**, *36*, 307.
57. Krebs, F. C. *Sol. Energy Mater. Sol.Cells* **2008**, *92*, 715.
58. Franke, R.; Maennig, B.; Petrich, A.; Pfeiffer, M. *Sol. Energy Mater. Sol. Cells* **2008**, *92*, 732.
59. Jørgensen, M.; Norrman, K.; Krebs, F. C. *Sol. Energy Mater. Sol.Cells* **2008**, *92*, 686.
60. Stübinger, T.; Brütting, W. *J. Appl. Phys.* **2001**, *90*, 3632.
61. Hoppe, H.; Sariciftci, N. S. *J. Mater. Res.***2004**, *19*, 1924.
62. Tang, C. W. *Appl. Phys. Lett.* **1986**, *48*, 183.
63. Peumans, P.; Forrest, S. R. *Appl. Phys. Lett.***2001**, *79*, 126.
64. Peumans, P.; Uchida, S.; Forrest, S. R. *Nature* (London) **2003**, *425*, 158.
65. Xue, J.; Uchida, S.; Rand, B. P.; Forrest, S. R. *Appl. Phys. Lett.* **2004**, *84*, 3013.
66. Xue, J.; Rand, B. P.; Uchida, S.; Forrest, S. R. *Adv. Mater.* **2005**, *17*, 66.
67. Rand, *Prog. Photovolt: Res. Appl.* **2007**, *15*, 659.
68. Chan, M. Y.; Lai, S. L.; Fung, M. K.; Lee; Lee, S. T. *Appl. Phys. Lett.* **2007**, *90*, 023504.
69. Yu, G.; Gao, J.; Hummelen, J. C.; Wudl, F.; Heeger, A. J. *Science* **1995**, *270*, 1789.
70. Yu, G.; Heeger, A. J. *J. Appl. Phys.* **1995**, *78*, 4510.
71. Shaheen, S. E.; Brabec, C. J.; Sariciftci, N. S.; Padinger, F.; Fromherz, T.; Hummelen, J. C. *Appl. Phys. Lett.* **2001**, *78*, 841.
72. Günes, S.; Neugebauer, H.; Sariciftci, N. S. *Chem. Rev.* **2007**, *107*, 1324.
73. Li, G.; Shrotriya, V.; Huang, J. S.; Yao, Y.; Moriarty, T.; Emery, K.; Yang, Y. *Nat. Mater.* **2005**, *4*, 864.
74. Ma, W. L; Yang, C. Y.; Gong, X.; Lee, K. H.; Heeger, A. J. *Adv. Funct. Mater.* **2005**, *15*, 1617.

75. Liang, Y.; Feng, D.; Wu, Y.; Tsai, S.-T.; Li, G.; Ray, C.; Yu, L. *J. Am. Chem. Soc.* **2009**, *131*, 7792.
76. Park, S. H.; Roy, A.; Beaupre, S.; Cho, S.; Coates, N.; Moon, J. S.; Moses, D.; Leclerc, M.; Lee, K.; Heeger, A. J. *Nat. Photonics* **2009**, *3*, 297.
77. Padinger, F.; Brabec, C. J.; Fromherz, T.; Hummelen, J. C.; Sariciftci, N. S. *Opto-Electron. Rev.* **2000**, *8*, 280.
78. Shaheen, S. E.; Radspinner, R.; Peyghambarian, N.; Jabbour, G. E. *Appl. Phys. Lett.* **2001**, *79*, 2996.
79. Hoth, C. S.; Choulis, S. A.; Schilinsky, P.; Brabec, C. J. *Adv. Mater.* **2007**, *19*, 3973.
80. Ishikawa, T.; Nakamura, M.; Fujita, K.; Tsutsui, T. *Appl. Phys. Lett.* **2004**, *84*, 2424.
81. El-Khouly, M. E.; Ito, O.; Smith, P. M.; D'Souza, F. *J. Photochem. Photobiol. C* **2004**, *5*, 79.
82. Owens, J. W.; Smith, R.; Robinson, R.; Robins, M. *Inorg. Chim. Acta* **1998**, *279*, 226.
83. Ermilov, E. A.; Tannert, S.; Werncke, T.; Choi, M. T. M.; Ng, D. K. P.; Röder, B. *Chem. Phys.* **2006**, *328*, 428.
84. Vehmanen, V.; Tkachenko, N. V.; Imahori, H.; Fukuzumi, S.; Lemmetyinen, H. *Spectrochim. Acta A* **2001**, *57*, 2229.
85. Ito, F.; Ishibashi, Y.; Khan, S. R.; Miyasaka, H.; Kameyama, K.; Morisue, M.; Satake, A.; Ogawa, K.; Kobuke, Y. *J. Phys. Chem. A* **2006**, *110*, 12734.
86. Monnereau, C.; Hidalgo Ramos, P.; Deutman, A. B. C.; Elemans, J. A. A. W.; Nolte, R. J. M.; Rowan, A. E. *J. Am. Chem. Soc.* **2010**, *132*, 1529.
87. Tagliatesta, P.; Giovannetti, D.; Leoni, A.; Neves, M. G. P. M. S.; Cavaleiro, J. A. S. *J. Mol. Cat. A: Chemical* **2006**, *252*, 96.
88. McNaught, A. D.; Wilkinson, A. *IUPAC. Compendium of Chemical Terminology, 2nd ed. (the "Gold Book")*; Blackwell Scientific Publications, Oxford, **1997**.
89. de la Torre, G.; Claessens, C. G.; Torres, T. *Chem. Commun.* **2007**, 2000.
90. Gebeyehu, D.; Maennig, D. B.; Drechsel, J.; Leo, K.; Pfeiffer, M. *Sol. Energy Mater. Solar Cells* **2003**, *79*, 81.

91. Koeppe, R.; Sariciftci, N. S.; Troshin, P. A.; Lyubovskaya, R. N. *Appl. Phys. Lett.***2005**, *87*, 244102.
92. Loi, M. A.; Denk, P.; Hoppe, H.; Neugebauer, H.; Meissner, D.; Winder, C.; Brabec, C. J.; Sariciftci, N. S.; Gouloumis, A.; Vásquez, P.; Torres, T. *Synth. Met.* **2003**, *137*, 1491.
93. Suemori, K.; Miyata, T.; Yokoyama, M.; Hiramoto, M. *Appl. Phys. Lett.* **2005**, 063509.
94. Hong, Z. R.; Maennig, B.; Lessmann, R.; Pfeiffer, M.; Leo, K. *Appl. Phys. Lett.***2007**, *90*, 203505.
95. Guldi, D. M.; Zilbermann, I.; Gouloumis, A.; Vásquez, P.; Torres, T. *J. Phys. Chem. B* **2004**, *108*, 18485.
96. Doyle, J. J.; Ballesteros, B.; de la Torre, G.; McGovern, D. A.; Kelly, J. M.; Torres, T.; Blau, W. J. *Chem. Phys. Lett.* **2006**, *428*, 307.
97. Ballesteros, B.; de la Torre, G.; Torres, T.; Hug, G. L.; Rahman, G. M. A.; Guldi, D. M. *Tetrahedron* **2006**, *62*, 2097.
98. Lehtivuori, H.; Kumpulainen, T.; Efimov, A.; Lemmetyinen, H.; Kira, A.; Imahori, H.; Tkachenko, N. V. *J. Phys. Chem. C* **2008**, *112*, 9896.
99. Ohkubo, K.; Fukuzumi, S. *J. Porphyrins Phthalocyanines* **2008**, *12*, 993.
100. Chandrasekhar, P. *Conducting Polymers, Fundamentals and Applications: A Practical Approach*, Springer, **1999**.
101. Vanlaeke, P.; Vanhoyland, G.; Aernouts, T.; Cheyns, D.; Deibel, C.; Manca, J.; Heremans, P.; Poortmans, J. *Thin Solid Films* **2006**, *511-512*, 358.
102. Kim, Y.; Cook, S.; Tuladhar, S. M.; Choulis, S. A.; Nelson, J.; Durrant, J. R.; Bradley, D. D. C.; Giles, M.; McCulloch, I.; Ha, C.-S.; Ree, M. *Nature Materials* **2006**, *5*, 197.
103. Kroto, H. W.; Heath, J. R.; O'Brien, S. C.; Curl, R. F.; Smalley, R. E. *Nature* **1985,** *318*, 162.
104. Kratschmer, W.; Lamb, L. D.; Fostiropoulos, K.; Huffman, D. R. *Nature* **1990**, *347*, 354.
105. Langa De la Puente, F.; Nierengarten, J-F. *Fullerenes: principles and applications*, RSC Publishing, **2007**.
106. Martín, N.; Sánchez, L.; Illescas, B.; Pérez, I. *Chem. Rev.* **1998**, *98*, 2527.
107. Prato, M. *J. Mater. Chem.* **1997**, *7*, 1097.

108. Liddell, P. A.; Sunida, J. P.; McPherson, A. N.; Noss, L.; Seely, G. R.; Clark, K. N.; Moore, A. L.; Moore, T. A.; Gust, D. *Photochem. Photobiol.* **1994**, *60*, 537.
109. Avlasevich, Y.; Li, C.; Müllen, K. *J. Mater. Chem.* **2010**, *20*, 3814.
110. Chesterfield, R. J.; Mekeer, J. C.; Newman, P. R.; Ewbank, P. C.; da Silva Filho, D. A.; Bredas, J. L.; Miller, L. L.; Mann, K. P.; Frisbie, C. D. *J. Phys. Chem. B* **2004**, *108*, 19281.
111. Hussain, S. A.; Paul, P. K.; Bhattacharjee, D. *J. Phys. Chem. Sol.***2006**, *67*, 2542.
112. Langhals, H.; Jona, W. *Angew. Chem., Int. Ed.**1998,** 37*, 952.
113. Langhals, H.; Poxleitner, S. *Eur. J. Org. Chem.* **2008**, *2008*, 797.
114. Angadi, M. A.; Gosztola, D.; Wasielewski, M. R. *Mater. Sci. Eng. B* **1999**, *63*, 191.
115. Ranke, P.; Bleyl, I.; Simmerer, J.; Haarer, D.; Bacher, A.; Schmidt, H. W. *Appl. Phys. Lett.* **1997**, *71*, 1332.
116. Li, J.; Kastler, M.; Pisula, W.; Robertson, J. W. F.; Wasserfallen, D.; Clive Grimsdale, A.; Wu, J.; Müllen, K. *Adv. Funct. Mater.***2007**, *17*, 2528.
117. Angadi, M. A.; Gosztola, D.; Wasielewski, M. R. *J. Appl. Phys.* **1998**, *83*, 6187.
118. Davis, W. B.; Svec, M. A.; Ratner, M. A.; Wasielewski, M. R. *Nature* **1998**, *396*, 60.
119. Lukas, A. S.; Bushard, P. J.; Wasielewski, M. R. *J. Am. Chem. Soc.* **2001**, *123*, 2440.
120. Law, K. Y. *Chem. Rev.* **1993**, *93*, 449.
121. Popovic, Z. D.; Loutfy, R. O.; Hor, A. M. *Can. J. Chem.* **1985**, *63*, 134.
122. Loutfy, R. O.; Tam, M.; Kazmaier, P. M.; Hor, A. M. *J. Imaging Sci.* **1989**, *33*, 151.
123. Schlettwein, D.; Woehrle, D.; Karmann, E.; Melville, U. *Chem. Mater*.**1994**, *6*, 3.
124. Schlettwein, D.; Armstrong, N. R. *J. Phys. Chem.* **1994**, *98*, 11771.
125. So, F. F.; Forrest, S. R. *Phy. Rev. Lett.* **1991**, *66*, 2649.
126. Grätzel, M. *Acc. Chem. Res.* **1981**, *14*, 376.
127. Bard, A. J.; Fox, M. A. *Acc. Chem. Res.* **1995**, *28*, 141.
128. Brune, A.; Jeong, G.; Liddell, P. A.; Sotomura, T.; Moore, T. A.; Moore, A. L.; Gust, D. *Langmuir* **2004**, *20*, 8366.

129. Imahori, H.; Kashiwagi, Y.; Hanada, T.; Endo, Y.; Nishimura, Y.; Yamazaki, I.; Fukuzumi, S. *J. Mater. Chem.* **2003**, *13*, 2890.
130. Campbell, W. M.; Burrell, A. K.; Officer, D. L.; Jolley, K. W. *Coord. Chem Rev.* **2004**, *248*, 1363.
131. Thomas, K. G.; George, M. V.; Kamat, P. V. *Helv. Chim. Acta*. **2005**, *88*, 1291.
132. D'Souza, F.; Ito, O. *Coord. Chem. Rev.* **2005**, *249*, 1410.
133. Tagmatarchis, N.; Prato, M. *Struct. Bond.* **2004**, *109*, 1.
134. Milanesio, M. E.; Gervaldo, M.; Otero, L. A.; Sereno, L.; Silber, J. J.; Durantini, E. N. *J. Phys. Org. Chem.* **2002**, *15*, 844.
135. Possamai, G.; Maggini, M.; Menna, E.; Scorrano, G.; Franco, L.; Ruzzi, M.; Corvaja, C.; Ridolfi, G.; Samorí, P.; Geri, A.; Camaioni, N. *Appl. Phys. A* **2004**, *79*, 51.
136. Neugebauer, H.; Loi, M. A.; Winder, C.; Sariciftci, N. S.; Cerullo, G.; Gouloumis, A.; Vásquez, P.; Torres, T. *Sol. Energy Mater. Sol. Cells* **2004**, *83*, 201.
137. Meng, F.; Hua, J.; Chen, K.; Tian, H.; Zuppiroli, F.; Nuesch, F. *J. Mater. Chem.* **2005**, *15*, 979.
138. Loi, M. A.; Denk, P.; Hoppe, H.; Neugebauer, H.; Winder, C.; Meissner, Brabec, C. J.; Sariciftci, N. S.; Gouloumis, A.; Vásquez, P.; Torres, T. *J. Mater. Chem.* **2003**, *13*, 700.
139. Maggini, M.; Possamai, G.; Menna, E.; Scorrano, G.; Camaioni, N.; Ridolfi, G.; Casalbore-Miceli, G.; Franco, L.; Ruzzi, M.; Corvaja, C. *Chem. Commun.* **2002**, *18*, 2028.
140. Yamada, H.; Imahori, H.; Nishimura, Y.; Yamazaki, I.; Ahn, T. K.; Kim, S. K.; Kim, D.; Fukuzumi, S. *J. Am. Chem. Soc.***2003**, *125*, 9129.
141. Nishizawa, T.; Kesuma Lim, H.; Tajima, K.; Hashimoto, K. *Chem. Commun.* **2009**, 2469.
142. Possamai, G.; Camaioni, N.; Ridolfi, G.; Franco, L.; Ruzzi, M.; Menna, E.; Casalbore-Miceli, G.; Fichera, A. M.; Scorrano, G.; Corvaja, C.; Maggini, M. *Synth. Met.* **2003**, *139*, 585.
143. Kuciauskas, D.; Liddell, P. A.; Lin, S.; Johnson, T. E.; Weghnorn, S. J.; Lindsey, J. S.; Moore, A. L.; Moore, T. A.; Gust, D. *J. Am. Chem. Soc.* **1999**, *121*, 8604.
144. Kodis, G.; Liddell, P. A.; de la Garza, L.; Clausem, P. C.; Lindsey, J. S.; Moore, A. L.; Moore, T. A.; Gust, D. *J. Phys.Chem. A* **2002**, *106*, 2036.

145. Kesti, T.; Tkachenko, N.; Yamada, H.; Imahori, H.; Fukuzumi, S.; Lemmetyinen, H. *Photochem. Photobiol. Sci* **2003**, *2*, 251.
146. Imahori, H.; Tkachenko, N. V.; Vehmanen, V.; Tamaki, K.; Lemmetyinen, H.; Sakata, Y.; Fukuzumi, S. *J. Phys. Chem. A* **2001**, *105*, 1750.
147. Chukharev, V.; Tkachenko, N. V.; Efimov, A.; Guldi, D. M.; Hirsch, A.; Scheloske, M.; Lemmetyinen, H. *J. Phys. Chem. B* **2004**, *108*, 16377.
148. Isosomppi, M.; Tkachenko, N. V.; Efimov, A.; Lemmetyinen, H.; *J. Phys. Chem. A* **2005**, *109*, 4881.
149. Kaunisto, K.; Chukharev, V.; Tkachenko, N. V.; Lemmetyinen, H. *Chem. Phys. Lett.* **2008**, *460*, 241.
150. Isosomppi, M.; Tkachenko, N. V.; Efimov, A.; Kaunisto, K.; Hosomizu, K.; Imahori, H.; Lemmetyinen, H. *J. Mater. Chem.* **2005**, *15*, 4546.
151. Isosomppi, M.; Tkachenko, N. V.; Efimov, A.; Vahasalo, H.; Jukola, J.; Vainotalo, P.; Lemmetyinen, H. *Chem. Phys. Lett.* **2006**, *430*, 36.
152. Niemi, M.; Tkachenko, N. V.; Efimov, A.; Lehtivuori, H.; Ohkubo, K.; Fukuzumi, S.; Lemmetyinen, H. *J. Phys. Chem. A* **2008**, *112*, 6884.
153. Bernède, J. C.; Cattin, L.; Morsli, M.; Berredjem, Y. *Sol. Energy Mater. Sol. Cells* **2008**, *92*, 1508.
154. Huang, J.; Miller, P. F.; Wilson, J. S.; de Mello, A. J.; de Mello, J. C.; Bradley, D. D. C. *Adv. Funct. Mater.* **2005**, *15*, 290.
155. Nardes, A. M.; Kemerink, M.; Janssen, R. A. J.; Bastiaansen, J. A. M.; Kiggen, N. M. M.; Langeveld, B. M. W.; van Breemen, A. J. J. M.; de Kok, M. M. *Adv. Mater.* **2007**, *19*, 1196.
156. Song, Q. L.; Li, F. Y.; Yang, H.; Wu, H. R.; Wang, X. Z.; Zhou, W.; Zhao, J. M.; Ding, X. M.; Huang, C. H.; Hou, X. Y. *Chem. Phys. Lett.* **2005**, *416*, 42.
157. Peumans, P.; Bulovic, V.; Forrest, S. R. *Appl. Phys. Lett.* **2000**, *76*, 2650.
158. Brabec, C. J.; Shaheen, S. E.; Winder, C.; Sariciftci, N. S.; Denk, P. *Appl. Phys. Lett.* **2002**, *80*, 1288.
159. Wang, N.; Yu. J.; Zang, Y.; Huang, J.; Jjang, Y. *Sol. Energy Mater. Sol. Cells* **2010**, *94*, 263.
160. Song, Q. L.; Li, C. M.; Wang, M. L.; Sun, X. Y.; Hou, X. Y. *Appl. Phys. Lett.* **2007**, *90*, 071109.

161. Chang, C.-C.; Lin, C.-F.; Chiou, J.-M.; Ho, T.-H.; Tai, Y.; Lee, J.-H.; Chen, Y.-F.; Wang, J.-K.; Chen, L.-C.; Chen, K.-H. *Appl. Phys. Lett.***2010**, *96*, 263506.
162. Zhang, F.; Ceder, M.; Inganäs, O. *Adv. Mater.* 2007, 19, 1835.
163. Yang, L.; Xu, H.; Tian, H.; Yin, S.; Zhang, F. *Sol. Energy Mater. Sol. Cells* **2010**, *94*, 1831.
164. Hong, Z. R.; Huang, Z. H.; Zeng, X. T. *Thin Solid Films* **2007**, *515*, 3019.
165. Efimov, A.; Vainotalo, P.; Tkachenko, N. V.; Lemmetyinen, H. *J. Porph. Phthaloc.* **2003**, *7*, 610.
166. Vuorinen, T.; Kaunisto, K.; Chukharev, V.; Tkachenko, N. V.; Efimov, A.; Lemmetyinen, H. *J. Phys. Chem. B* **2006**, *110*, 19515.
167. Petty, M. C. *Langmuir–Blodgett films: An Introduction*, Cambridge University Press, **1996**.
168. Vuorinen, T.; Kaunisto, K.; Tkachenko, N. V.; Efimov, A.; Alekseev, A. S.; Hosomizu, K.; Imahori, H.; Lemmetyinen, H. *Langmuir* **2005**, *21*, 5383.
169. Alekseev, A. S.; Tkachenko, N. V.; Tauber, A. Y.; Hynninen, P. H.; Osterbacka, R.; Stubb, H.; Lemmetyinen, H. *Chem. Phys.* **2002**, *275*, 243.
170. Tkachenko, N. V.; Tauber, A. Y.; Hynninen, P. H.; Sharonov, A. Y.; Lemmetyinen, H. *J. Phys. Chem. A* **1999**, *103*, 3657.
171. Tkachenko, N. V.; Vuorimaa, E.; Kesti, T.; Alekseev, A. S.; Tauber, A. Y.; Hynninen, P. H.; Lemmetyinen, H. *J. Phys. Chem. B* **2000**, *104*, 6371.
172. Tkachenko, N. V.; Vehmanen, V., Efimov, A.; Alekseev, A. S.; Lemmetyinen, H. *J. Porph. Phthaloc.* **2003**, *7*, 255.
173. Chukharev, V.; Vuorinen, T.; Efimov, A.; Tkachenko, N. V.; Kimura, M.; Fukuzumi, S.; Imahori, H.; Lemmeytinen, H. *Langmuir* **2005**, *21*, 6385.
174. Kotiaho, A.; Lahtinen, R. M.; Tkachenko, N. V.; Efimov, A.; Kira, A.; Imahori, H.; Lemmetyinen, H. *Langmuir* **2007**, *23*, 13117.
175. Tkachenko, N. V.; Hynninen, P. H.; Lemmetyinen, H. *Chem. Phys. Lett.* **1996**, *261*, 234.
176. Manoi, A. G.; Narayan, K. S. *Opt. Mater.* **2002**, *21*, 417.
177. Chiechi, R. C.; Weiss, E. A.; Dickey, M. D.; Whitesides, G. M. *Angew. Chem.* **2008**, *120*, 148.

178. Moliton, A.; Nunzi, J. M. *Polym Int* **2006**, *55*, 583.
179. Roberts, G. G. *Languir–Blodgett Films*, Plenum Press, New York, **1990**.
180. Kotiaho, A.; Lahtinen, R. M.; Latvala, H.-K.; Efimov, A.; Tkachenko, N. V.; Lemmetyinen, H. *Chem. Phys. Lett.* **2009**, *471*, 269.
181. Lehtivuori, H.; Kumpulainen, T.; Hietala, M.; Efimov, A.; Lemmetyinen, H.; Kira, A.; Imahori, H.; Tkachenko, N. V. *J. Phys. Chem. C* **2009**, *113*, 1984.
182. Yun, J-J.; Jung, H-S.; Kim, S-H.; Han, E-M.; Vaithianathan, V.; Jenekhe, S.A. *Appl. Phys. Lett.* **2005**, *87*, 123102.
183. Chen, L. L.; Li, W. L.; Wei, H. Z.; Chu, B.; Li, B. *Sol. Energy. Mater. Sol. Cells* **2005**, *90*, 1788.
184. Rand, B.; Burk, D. *Physical Review B* **2007**, *75*, 115327.
185. Chiş, V.; Mile, G.; Ştiufiuc, R.; Leopold, N.; Oltean, M. *J. of Mol. Struct.* **2009**, *924-926*, 47.
186. Pommerehne, J.; Vestweber, H.; Guss, W.; Mahrt, R. F.; Bässler, H.; Porsch, M.; Daub, J. *Adv. Mater.* **1995**, *7*, 551.
187. Lide, D. R. *Handbook of Chemistry and Physics*, 90th edition, CRC (Taylor & Francis group), **2010**.
188. Murtaza, I.; Qazi, I.; Karimov, K. S. *J. Semicond.* **2010**, *31*(6), 064005.
189. Seudi, R.; El-Bahy, G. S.; El-Sayed, Z. A. *Opt. Mater.* **2006**, *29*, 304.
190. Lehtivuori, H.; Efimov, A.; Lemmetyinen, H.; Tkachenko, N. V. *Chem. Phys. Lett.* **2007**, *437*, 238.
191. Imahori, H.; El-Khouly, M. E.; Fujitsuka, M.; Ito, O.; Sakata, Y.; Fukuzumi, S. *J. Phys. Chem. A* **2001**, *105*, 325.
192. Gosztola, D.; Niemczyk, M. P.; Svec, W.; Lukas, A. S.; Wasielewski, S. *J. Phys. Chem. A* **2000**, *104*, 6545.
193. Fukuzumi, S.; Ohkubo, K.; Ortiz, J.; Gutiérrez, A. M.; Fernández-Lázaro, F.; Sastre-Santos, A. *J. Phys. Chem. A* **2008**, *112*, 10744.
194. van der Boom, T.; Hayes, R. T.; Zhao, Y.; Bushard, P. J.; Weiss, E. A.; Wasielewski, M. R. *J. Am. Chem. Soc.* **2002**, *124*, 9582.
195. Baffreau, J.; Leroy-Lhez, S.; Hudhomme, P.; Groeneveld, M. M.; van Stokkum, I. H. M.; Williams, R. M. *J. Phys. Chem. A* **2006**, *110*, 13123.
196. Johansoon, E. M. J.; Yartzev, A; Rensmo, H.; Sundström, V. *J. Phys. Chem. C* **2009**, *113*, 3014.

197. Li, J.; Osasa, T.; Hirayama, Y.; Sano, T.; Wakisaka, K.; Matsumura, M. *Sol. Energy Mater. Sol. Cells* **2007**, *91*, 745.
198. Kawano, K.; Pacios, R.; Poplavskyy, D.; Nelson, J.; Bradley, D.; Durrant, J. *Sol. Energy Mater. Sol. Cells* **2006**, *90*, 3520.
199. Sahin, Y.; Alem, S.; de Bettignies, R.; Nunzi, J. M. *Thin Solid Films* **2005**, *476*, 340.
200. Ishii, H.; Sugiyama, K.; Ito, E.; Seki, K. *Adv. Mater.* **1999**, *11*, 605.
201. Limketkai, B. N.; Baldo, M. A. *Phys. Rev. B* **2005**, *71*, 085207.
202. Gust, D.; Moore, T. A. *Science* **1989**, *244*, 35.
203. Wasielewski, M. R. *Chem. Rev.* **1992**, *92*, 435.
204. Luo, C.; Guldi, D. M.; Imahori, H.; Tamaki, K.; Sakata, Y. *J. Am. Chem. Soc.* **2000**, *122*, 6535.
205. Imahori, H.; Mori, Y.; Matano, Y. *J. Photochem. Photobiol. C* **2003**, *4*, 51.
206. D'Souza, F.; Smith, P. M.; Gadde, S.; McCarty, A. L.; Kullman, M. J.; Zendler, M. E.; Itou, M.; Araki, Y.; Ito, O. *J. Phys. Chem. B* **2004**, *108*, 11333.
207. Koeppe, R.; Bossart, O.; Calzaferri, G.; Sariciftci, N. S. *Sol. Energy Mater. Sol. Cells* **2007**, *91*, 986.
208. Koeppe, R.; Sariciftci, N. S.; Büchtemann, A. *Appl. Phys. Lett.* **2007**, *90*, 181126.
209. Ranta, J.; Kumpulainen, T.; Lemmetyinen, H.; Efimov, A. *J. Org. Chem.* **2010**, *75*, 5178.